Resource Estimation for VQE on Small Molecules: Impact of Fermion Mappings and Hamiltonian Reductions

Anurag K. S. V.[1], **Ashish Kumar Patra**[1], **Vikas Dattatraya Ghevade**[1, 2], **Sai Shankar P.**[1], **Ruchika Bhat**[1, 3], **Raghavendra V.**[4], **Rahul Maitra**[2], **and Jaiganesh G.**[*, 1]

[1]Qclairvoyance Quantum Labs, Secunderabad, TG 500094, India.
[2]Indian Institute of Technology Bombay, Mumbai, MH 400076, India.
[3]The University of Arizona, Tucson, AZ 85721, USA.
[4]SRM Institute of Science and Technology, Chennai, TN 603203, India.

ABSTRACT

Accurate determination of ground-state energies for molecules remains a challenge in quantum chemistry and a cornerstone for progress in fields such as drug discovery and materials design. The Variational Quantum Eigensolver (VQE) represents a leading hybrid quantum-classical paradigm for addressing this challenge; however, its widespread realization is limited by noise and the restricted scalability of current quantum hardware. Achieving efficient simulations on Noisy Intermediate-Scale Quantum (NISQ) devices and forthcoming Fault-Tolerant Application-Scalable Quantum (FASQ) systems demands a detailed understanding of how computational resources scale with molecular complexity and fermion-to-qubit encoding schemes. In this study, resource requirements for VQE implementations employing the Unitary Coupled Cluster Singles and Doubles (UCCSD) ansatz are systematically analyzed. The molecular Hamiltonian is formulated in second quantization and mapped to qubit operators through the Jordan-Wigner (JW), Bravyi-Kitaev (BK), and Parity (Pa) transformations. Hamiltonian reduction strategies, including $\mathbb{Z}_2$ tapering and frozen-core approximations, are examined to assess their effect on quantum resource scaling. The analysis reveals that appropriate transformations, when combined with symmetry-based reductions, can substantially reduce qubit counts by up to $\approx 50\%$ and quantum gate counts by up to $\approx 27.5\times$ and Hamiltonian Pauli string counts by up to $\approx 2.75\times$, relative to the corresponding unreduced Hamiltonian representations within the same active-space configuration for the representative set of molecular systems under study. These findings provide practical circuit-level insights for executing chemically relevant simulations on NISQ hardware, while establishing physical-resource baselines that may inform future logical-level analyses targeting FASQ systems.

Keywords: Quantum Computing · Quantum Algorithms · Resource Estimation · Fermion-to-Qubit Mapping · Hamiltonian Reduction · VQE · UCCSD

[*]email: jaiganesh@qclairvoyance.in, drjaiganesh15@gmail.com (Corresponding Author)

1 Introduction

Quantum computing (QC) is poised to transform computational paradigms by exploiting quantum-mechanical phenomena such as quantum superposition[1,2], quantum interference[3,4], and quantum entanglement[5,6] to perform computation using qubits rather than classical bits[2,7–10]. Several classes of quantum algorithms have demonstrated theoretical promise in addressing problems in simulation[2,11,12], optimization[13,14], and search[8,15]. Among the most compelling early applications is quantum-assisted molecular modelling, where quantum computers are employed to solve the electronic structure problem[16–18] by evaluating the expectation value of the molecular Hamiltonian[17,19] acting on the molecular wavefunction.

The Quantum Phase Estimation (QPE) algorithm provides an asymptotically optimal, fully quantum method for extracting the eigenvalues of the Hamiltonian by coherently simulating its time evolution and performing an inverse quantum Fourier transform-based phase readout[12,20]. Although QPE enables chemically accurate energy estimation with polynomial scaling, its implementation requires deep circuits, long coherence times, and fault-tolerant error correction. These requirements limit its near-term applicability on NISQ[21] hardware and underscore the long-term need for FASQ[22] devices. The VQE algorithm, on the other hand, approximates the ground-state energy of the given Hamiltonian by preparing parameterized quantum circuits (ansätze) and iteratively optimizing their parameters using classical optimizer feedback loops[23,24]. A widely adopted chemistry-inspired ansatz is the UCCSD ansatz[25], which provides a physically motivated way to represent correlated electronic wavefunctions on QC hardware. The practical realization of VQE with UCCSD remains strongly constrained by the current state of QC hardware, which is dominated by noise, limited connectivity, and shallow circuit depths characteristic of the NISQ era[26].

Given these engineering challenges and the limited hardware availability of NISQ and the long-term development of FASQ devices, a priori resource estimation is essential for assessing the scale of quantum circuits that can be realistically executed. Recent research has examined the algorithmic components that fundamentally determine the resource demands of quantum chemistry simulations, particularly for small-molecule VQE workflows. Foundational comparisons of fermion-to-qubit mappings (FTQMs) across 86 molecular systems have shown that the BK transformation often reduces Pauli string lengths and gate counts relative to the JW mapping, offering tangible savings for NISQ hardware implementations[27]. Complementary investigations of UCCSD-VQE accuracy on small molecules demonstrated that the method can capture chemically meaningful energies for both open- and closed-shell species, while also highlighting that practical usefulness depends on the attainable qubit counts, circuit depths, and noise levels of NISQ devices[28]. Beyond chemistry problems, broader VQE resource studies, such as those for the Hubbard model, have underscored the scaling bottlenecks associated with two-qubit operations and measurement shot requirements, showing that meaningful simulations of 50-qubits already require tens of thousands of entangling gates and low two-qubit-gate-error rates ($\sim 10^{-4}$)[29]. These insights collectively emphasize that, even before algorithmic optimization, Hamiltonian structure, mapping choice, and ansatz construction are major determinants of VQE feasibility.

Further work has focused on quantifying and reducing the dominant runtime overheads associated with measurement, optimization, and Hamiltonian evaluation. Robust amplitude-estimation-based measurement protocols have been shown to reduce the shot complexity of VQE energy estimation by one to two orders of magnitude compared with standard sampling strategies, though they remain impractically demanding for many chemical systems[30]. Parallel efforts have produced resource-estimation tools, such as QREChem, which analyze logical gate counts for Trotterized QPE and provide baselines for molecules ranging from 10^7 to 10^{15} T gates, illustrating the enormous gap between NISQ and FASQ requirements[31]. The measurement overhead associated with evaluating the expectation value of the Hamiltonian in VQE represents a well-recognised practical bottleneck[32,33]. The number of required measurement circuits scales with the number of unique Pauli strings in the Hamiltonian, and achieving chemically meaningful precision requires large numbers of circuit repetitions, a cost that grows with system size. Reviews on quantum-chemistry measurement strategies for VQE and QPE[34], as well as practical hardware studies evaluating UCCSD versus hardware-efficient ansätze on IBM Quantum hardware[35], further highlight that measurement grouping, symmetry exploitation, and noise-robust ansatz choices are essential for molecule simulations on QC hardware. More broadly, recent assessments of quantum advantage in computational chemistry[36] and perspectives on 25 to 100 logical-qubit early FASQ devices[37] suggest that quantum chemistry will remain a leading candidate for early utility, but only with careful co-design of resource-aware algorithms and chemically relevant problem instances. Together, these works establish resource estimation not only as a forecasting tool but also as a design principle, central to evaluating the realistic prospects of QC simulations for small-molecule electronic structure calculations.

In this work, we perform a systematic, hardware-agnostic quantum-resource analysis of VQE with the UCCSD ansatz for a representative set of small molecules: H_2, LiH, HF, BeH_2, H_2O, N_2, O_2, CO, NH_3, CH_4, C_2H_2, H_2O_2, and C_2H_4, on QC simulators, thereby isolating mapping-dependent effects from hardware-specific compilation constraints. To enable a balanced and consistent comparison across fermion-to-qubit mappings, we adopt the UCCSD ansatz as a static, chemically motivated, and systematically improvable reference framework that remains independent of hardware topology. Hardware-efficient ansatz (HEA)[38,39] and adaptive ansatz (ADAPT)[40,41] constructions can significantly reduce circuit depth relative to UCCSD. However, these adaptive schemes require substantial additional measurement overhead during ansatz construction. Recent developments,

including measurement-efficient ansatz strategies such as COMPASS[42] and COMPASS-PRO[43], SURGE-VQE[44], as well as approaches such as COMPACT[45] and RBM-VQE[46,47] have partially or fully alleviated these costs. While UCCSD is known to generate deeper circuits than hardware-efficient, adaptive, and measurement-efficient alternatives, the resulting circuit metrics may be interpreted as representative upper bounds on resource requirements within the single- and double-excitation manifolds of a chemically motivated ansatz framework. A systematic evaluation of hardware-efficient, adaptive, and measurement-efficient ansatz families is therefore outside the scope of the present study.

The resource metrics reported here are physical circuit-level quantities after transpilation, directly relevant to NISQ and near-term quantum hardware. Logical-level resource estimates, including logical qubit counts, T-gate counts, and error-correction overheads, as well as full measurement-cost analysis, including shot-count and Pauli grouping overheads, are outside the scope of this work but represent a natural extension of the baselines established here. Concretely, we (1) quantify qubit counts, Pauli string counts, and quantum gate counts, across common FTQMs[17], and (2) evaluate the impact of the frozen-core approximation[48] and $\mathbb{Z}_2$-symmetry-based qubit tapering[49] on reducing resource requirements. The theoretical background of the work is outlined in Section 2, followed by the methodology employed in Section 3. The results and their discussion are presented in Section 4, and the concluding remarks are provided in Section 5.

2 Theoretical Background

Accurate quantum simulation of molecular systems requires a rigorous formulation of the molecular Hamiltonian and its associated wavefunction, followed by a sequence of transformations that render the problem suitable for execution on quantum hardware. Starting from the non-relativistic molecular Hamiltonian $\hat{H}_{mol}$ and the molecular wavefunction $\psi(\vec{r},\vec{R})$ (Section 2.1), the problem is systematically reduced to an effective electronic Hamiltonian $\hat{H}_{elec}$ and electronic wavefunction $\psi_e(\vec{r};\vec{R})$ (Section 2.2). The Hamiltonian $\hat{H}_{elec}$ is then expressed in its second-quantized fermionic form $\hat{H}_{sq}$ with the corresponding state $|\psi_{sq}\rangle$ (Section 2.3). Subsequently, $\hat{H}_{sq}$ is mapped to a qubit Hamiltonian $\hat{H}_{qubit}$, and the state $|\psi_{sq}\rangle$ is transformed to the qubit basis to obtain $|\Psi_{qubit}\rangle$ (Section 2.4) using FTQMs such as JW[50,51], BK[52–54], and Pa[17,53] (Section 2.5). This enables quantum simulation of the molecular system on universal gate-based quantum computers. To further enhance simulation efficiency, Hamiltonian reduction techniques, such as freezing core orbitals to obtain $\hat{H}_{fc}$ and tapering symmetries to derive the symmetry-reduced Hamiltonian $\hat{H}_{tapered}$, may be applied (Section 2.6).

2.1 Non-relativistic Molecular Hamiltonian and Wavefunction

Within the framework of non-relativistic quantum mechanics[55], the total energy of a molecular system is represented by the Hamiltonian operator, which can be expressed as the sum of its kinetic energy and potential energy:

$$\hat{H} = \hat{T} + \hat{V}, \tag{1}$$

where the total kinetic energy operator $\hat{T}$ in Eq. (1) consists of the nuclear $\hat{T}_N$ and the electronic $\hat{T}_e$ contributions:

$$\hat{T} = \hat{T}_N + \hat{T}_e; \quad \hat{T}_N = -\sum_{A=1}^{N_n} \frac{\hbar^2}{2M_A}\hat{\nabla}_A^2, \quad \hat{T}_e = -\sum_{i=1}^{N_e} \frac{\hbar^2}{2m_e}\hat{\nabla}_i^2, \tag{2}$$

and the potential energy operator $\hat{V}$ in Eq. (1) consists of all the Coulomb interactions present in the molecular system. These consist of the electron–nuclear ($\hat{V}_{eN}$), electron–electron ($\hat{V}_{ee}$), and nuclear–nuclear ($\hat{V}_{NN}$) interactions:

$$\hat{V} = \hat{V}_{eN} + \hat{V}_{ee} + \hat{V}_{NN}; \quad \hat{V}_{eN} = -\sum_{i=1}^{N_e}\sum_{A=1}^{N_n} \frac{Z_A \cdot e^2}{|\vec{r}_{iA}|}, \quad \hat{V}_{ee} = \frac{1}{2}\sum_{\substack{i,j \\ i\neq j}}^{N_e} \frac{e^2}{|\vec{r}_{ij}|}, \quad \hat{V}_{NN} = \frac{1}{2}\sum_{\substack{A,B \\ A\neq B}}^{N_n} \frac{Z_A \cdot Z_B \cdot e^2}{|\vec{R}_{AB}|}, \tag{3}$$

combining these components from Eqs. (2) and (3) yields the standard non-relativistic molecular Hamiltonian $\hat{H}_{mol}$ in atomic units[55]:

$$\hat{H}_{mol} = -\sum_{A=1}^{N_n} \frac{1}{2M_A}\hat{\nabla}_A^2 - \sum_{i=1}^{N_e} \frac{1}{2}\hat{\nabla}_i^2 - \sum_{i=1}^{N_e}\sum_{A=1}^{N_n} \frac{Z_A}{|\vec{r}_{iA}|} + \frac{1}{2}\sum_{\substack{i,j \\ i\neq j}}^{N_e} \frac{1}{|\vec{r}_{ij}|} + \frac{1}{2}\sum_{\substack{A,B \\ A\neq B}}^{N_n} \frac{Z_A \cdot Z_B}{|\vec{R}_{AB}|}, \tag{4}$$

In Eqs. (2), (3), and (4), $\hbar = h/2\pi$, where h is Planck's constant. $\hat{\nabla}_A^2$ and $\hat{\nabla}_i^2$ denote the Laplacian operators corresponding to nucleus A and electron i, respectively. N_e and N_n represent the numbers of electrons and nuclei; $Z_A(Z_B)$ and M_A correspond to the atomic number and mass of nucleus $A(B)$; m_e is the mass of an electron; and e is the elementary charge. $|\vec{r}_{iA}|$, $|\vec{r}_{ij}|$, and $|\vec{R}_{AB}|$ denote the electron-nucleus, electron-electron, and nucleus-nucleus separations, respectively, as shown in Figure 1. In

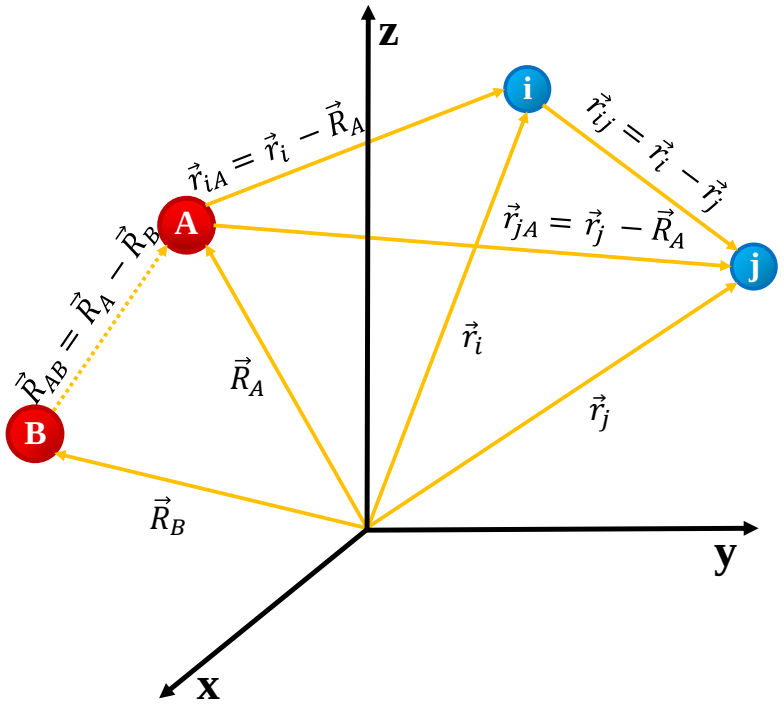

Figure 1. Schematic representation of a diatomic molecular system described by the non-relativistic molecular Hamiltonian in Eq. (4). The nuclei A and B (shown in red) and electrons i and j (shown in blue) are located by their respective position vectors $\vec{R}_A, \vec{R}_B, \vec{r}_i$, and $\vec{r}_j$ with respect to the origin. The inter-particle vectors $\vec{r}_{iA}, \vec{r}_{jA}$, and $\vec{r}_{ij}$ are represented as solid lines, while the internuclear vector $\vec{R}_{AB} = \vec{R}_A - \vec{R}_B$ is shown as a dotted line to indicate that, under the Born–Oppenheimer approximation, the internuclear separation is treated as a fixed parameter.

Eq. (4), the first two terms describe the nuclear and electronic kinetic energy operators ($\hat{T}_N$ and $\hat{T}_e$), the third term represents the electron–nucleus attraction ($\hat{V}_{eN}$), the fourth term corresponds to the electron–electron repulsion ($\hat{V}_{ee}$), and the final term accounts for the nucleus–nucleus repulsion ($\hat{V}_{NN}$).

The total molecular wavefunction $\psi(\vec{r},\vec{R})$ is defined over both the electronic coordinates $\vec{r} = (\vec{r}_1, \vec{r}_2, \ldots, \vec{r}_{N_e})$ and the nuclear coordinates $\vec{R} = (\vec{R}_1, \vec{R}_2, \ldots, \vec{R}_{N_n})$[55,56]:

$$\psi(\vec{r},\vec{R}) = \psi(\vec{r}_1, \vec{r}_2, \ldots, \vec{r}_{N_e}, \vec{R}_1, \vec{R}_2, \ldots, \vec{R}_{N_n}). \tag{5}$$

This wavefunction encompasses all dynamical variables of the system, including the correlated motion of electrons and nuclei, within the Born-Huang representation[57].

Accordingly, the molecular energy E_{mol} is obtained by solving the time-independent molecular Schrödinger equation:

$$\hat{H}_{mol}\, \psi(\vec{r},\vec{R}) = E_{mol}\, \psi(\vec{r},\vec{R}), \tag{6}$$

where $\hat{H}_{mol}$ is the non-relativistic molecular Hamiltonian defined in Eq. (4). The molecular wavefunction $\psi(\vec{r},\vec{R})$ is antisymmetric under exchange of any two electrons, consistent with the Pauli exclusion principle[55,56,58,59].

This formulation, referred to as the first-quantized molecular Hamiltonian, provides the foundation for further approximations such as the Born-Oppenheimer (B.O.) separation of electronic and nuclear motion, leading to the first-quantized electronic Hamiltonian $\hat{H}_{elec}$[60]. While the B.O. separation provides a practical and widely used route to electronic-structure calculations, several non-B.O. frameworks, such as the early protonic-structure[61,62], nuclear-orbital plus molecular-orbital (NOMO)[63–67], multicomponent molecular-orbital (MCMO)[68,69], nuclear-electronic orbital (NEO)[70,71], and more recent constrained NEO (CNEO)[72–74], treat electrons and selected nuclei quantum mechanically. A detailed treatment of these non-B.O. formulations, although essential for fully correlated nuclear-electronic dynamics, lies beyond the scope of the present work. Here, we focus on $\hat{H}_{mol}$ derived under the B.O. approximation, yielding $\hat{H}_{elec}$ as discussed in the next section.

2.2 Electronic Hamiltonian and Wavefunction

To simplify the many-body system in Eq. (4), the B.O. approximation assumes that nuclei remain effectively stationary due to their much larger masses compared to electrons. Consequently, the nuclear kinetic energy term $\hat{T}_N$ can be neglected, and the nuclei are treated as fixed classical point charges[55–57,60].

The resulting first-quantized electronic Hamiltonian $\hat{H}_{elec}$, parametrized by the nuclear coordinates $\vec{R}$, is expressed as:

$$\hat{H}_{elec} = -\frac{1}{2}\sum_{i=1}^{N_e}\hat{\nabla}_i^2 - \sum_{i=1}^{N_e}\sum_{A=1}^{N_n}\frac{Z_A}{|\vec{r}_{iA}|} + \frac{1}{2}\sum_{\substack{i,j\\ i\neq j}}^{N_e}\frac{1}{|\vec{r}_{ij}|} + \hat{V}_{NN}, \tag{7}$$

where $\hat{V}_{NN} = \frac{1}{2}\sum_{\substack{A,B\\ A\neq B}}^{N_n}\frac{Z_A Z_B}{|\vec{R}_{AB}|}$ represents the constant nuclear–nuclear repulsion energy.

The corresponding electronic wavefunction depends explicitly on the electronic coordinates $\vec{r} = (\vec{r}_1, \vec{r}_2, \ldots, \vec{r}_{N_e})$ and parametrically on the nuclear coordinates $\vec{R}$. Incorporating spin, each electron is described by combined space–spin coordinates $\chi_i = (\vec{r}_i, \sigma_i)$, where $\sigma_i \in \{\uparrow, \downarrow\}$. The complete electronic wavefunction $\psi_e(\chi;\vec{R})$ is therefore given by:

$$\psi_e(\chi;\vec{R}) = \psi_e(\chi_1, \chi_2, \ldots, \chi_{N_e};\vec{R}). \tag{8}$$

The electronic energy at a fixed nuclear configuration $E_{elec}(\vec{R})$ is obtained by solving the time-independent electronic Schrödinger equation:

$$\hat{H}_{elec}(\vec{R})\,\psi_e(\chi;\vec{R}) = E_{elec}(\vec{R})\,\psi_e(\chi;\vec{R}), \tag{9}$$

where $\hat{H}_{elec}(\vec{R})$ is the electronic Hamiltonian for a given nuclear geometry $\vec{R}$.

However, operating directly in the continuous first-quantized coordinate representation of $\hat{H}_{elec}$ and $\psi_e(\chi;\vec{R})$ is computationally inefficient for many-body systems. To enable efficient numerical treatment and facilitate quantum simulation, the Hamiltonian is reformulated in second quantization as $\hat{H}_{sq}$, where the wavefunction of the system is expressed in the discrete occupation-number basis as $|\psi_{sq}\rangle$. In this representation, the Hamiltonian is written in terms of fermionic creation and annihilation operators $(\hat{a}^\dagger, \hat{a})$, as discussed in detail in the following section.

2.3 Second Quantization: Fermionic Representation

In the second-quantized framework, the first-quantized electronic Hamiltonian $\hat{H}_{elec}$ is expressed as:

$$\hat{H}_{sq} = \sum_{pq} h_{pq}\,\hat{a}_p^\dagger \hat{a}_q + \frac{1}{2}\sum_{pqrs} h_{pqrs}\,\hat{a}_p^\dagger \hat{a}_q^\dagger \hat{a}_r \hat{a}_s, \tag{10}$$

where $\hat{a}_p^\dagger$ and $\hat{a}_q$ are the $(\hat{a}^\dagger, \hat{a})$ acting on spin orbitals labeled by indices p and q. These operators obey the canonical anti-commutation relations[55,56]:

$$\{\hat{a}_p^\dagger, \hat{a}_q\} = \delta_{pq}, \quad \{\hat{a}_p, \hat{a}_q\} = 0, \quad \{\hat{a}_p^\dagger, \hat{a}_q^\dagger\} = 0. \tag{11}$$

The coefficients h_{pq} and h_{pqrs} represent the one- and two-electron integrals evaluated over the selected spin orbital basis. The one-electron integrals are given by:

$$h_{pq} = \int d\vec{r}\,\xi_p^*(\vec{r})\left[-\frac{1}{2}\hat{\nabla}^2 - \sum_{A=1}^{N_n}\frac{Z_A}{|\vec{r}-\vec{R}_A|}\right]\chi_q(\vec{r}), \tag{12}$$

incorporate the electronic kinetic energy and electron–nucleus attraction, where $\xi_p(\vec{r})$ is the spin orbital for index p, Z_A represents the atomic number associated with A, $\vec{R}_A$ is its position. The two-electron integrals:

$$h_{pqrs} = \int\int d\vec{r}_1 d\vec{r}_2 \frac{\xi_p^*(\vec{r}_1)\xi_q^*(\vec{r}_2)\xi_r(\vec{r}_1)\xi_s(\vec{r}_2)}{|\vec{r}_1 - \vec{r}_2|}, \tag{13}$$

account for electron-electron repulsion. The prefactor $1/2$ in Eq. (10) avoids double counting over electron pairs.

The indices p, q, r, s span the complete set of spin orbitals in the chosen basis (e.g., STO-3G[75], cc-pVDZ[76]). The resulting operator $\hat{H}_{sq}$ acts on Fock space[77], a discrete Hilbert space spanned by the occupation-number basis:

$$|n_{m-1}\rangle \otimes |n_{m-2}\rangle \otimes \ldots \otimes |n_1\rangle \otimes |n_0\rangle, \qquad n_j \in \{0,1\}, \tag{14}$$

where m denotes the total number of spin orbitals, and $|n_j\rangle$ denotes whether the j^{th} spin orbital is occupied. The many-electron wavefunction in its second quantized form $|\psi_{sq}\rangle$ is then expressed as a superposition of these occupation-number basis states:

$$|\psi_{sq}\rangle = \sum_j c_j \bigotimes_{k=0}^{m-1} |n_k\rangle = \sum_j c_j |\phi_j\rangle, \quad n_k \in \{0,1\}, \tag{15}$$

where c_j are the probability amplitudes of the basis states $|\phi_j\rangle$ expressed in occupation number basis (Eq. (14)). The time-independent electronic Schrödinger equation in occupation-number basis is given as:

$$\hat{H}_{sq}(\vec{R})\,|\psi_{sq}\rangle = E_{elec}(\vec{R})\,|\psi_{sq}\rangle \tag{16}$$

where, $H_{sq}(\vec{R})$ is second quantized electronic Hamiltonian for the given nuclear geometry $\vec{R}$.

This fermionic representation $\hat{H}_{sq}$ forms the bridge between $\hat{H}_{elec}$ and its qubit-based encoding via mappings that transform fermionic operators into qubit operators suitable for implementation on QC hardware. The resulting qubit Hamiltonian $\hat{H}_{qubit}$ serves as the input to quantum algorithms, discussed in the next section.

2.4 Qubit Hamiltonian and Wavefunction

The second-quantized Hamiltonian, $\hat{H}_{sq}$, can subsequently be transformed into the $\hat{H}_{qubit}$, represented as a linear combination of tensor products of Pauli operators ($\hat{\sigma}_x$, $\hat{\sigma}_y$, $\hat{\sigma}_z$) and the identity operator $\hat{\mathbb{I}}_2$:

$$\hat{\sigma}_x = \begin{bmatrix} 0 & 1 \\ 1 & 0 \end{bmatrix}, \quad \hat{\sigma}_y = \begin{bmatrix} 0 & -i \\ i & 0 \end{bmatrix}, \quad \hat{\sigma}_z = \begin{bmatrix} 1 & 0 \\ 0 & -1 \end{bmatrix}, \quad \hat{\mathbb{I}}_2 = \begin{bmatrix} 1 & 0 \\ 0 & 1 \end{bmatrix}. \tag{17}$$

This transformation is performed through FTQMs such as JW, BK, and Pa. These mappings yield the $\hat{H}_{qubit}$:

$$\hat{H}_{qubit} = \sum_j \tau_j \bigotimes_{k=0}^{m-1} \hat{\sigma}_p^k, \quad \hat{\sigma}_p \in \{\hat{\sigma}_x, \hat{\sigma}_y, \hat{\sigma}_z, \hat{\mathbb{I}}_2\}, \tag{18}$$

where $\bigotimes_{k=0}^{m-1} \hat{\sigma}_p^k$ are the Pauli strings of $\hat{H}_{qubit}$ and τ_j are the co-efficients of the Pauli strings. The corresponding statevector representation of the wavefunction $|\Psi_{qubit}\rangle$ takes the form:

$$|\Psi_{qubit}\rangle = \sum_j c_j \bigotimes_{k=0}^{m-1} |q_k\rangle = \sum_j c_j |\Phi_j\rangle, \quad q_k \in \{0,1\}, \tag{19}$$

where, c_j are the probability amplitudes corresponding to the computational basis states $|\Phi_j\rangle$. $|\Phi_j\rangle$ is given as $\bigotimes_{k=0}^{m-1} |q_k\rangle$, and $|q_k\rangle$ denotes the state of the k^{th} qubit. Therefore, the general time-independent electronic Schrödinger equation given $\hat{H}_{qubit}$ and $|\Psi_{qubit}\rangle$ is expressed as:

$$\hat{H}_{qubit}(\vec{R})\,|\Psi_{qubit}\rangle = E_{elec}(\vec{R})\,|\Psi_{qubit}\rangle, \tag{20}$$

where, $\hat{H}_{qubit}(\vec{R})$ is the qubit Hamiltonian for a given nuclear geometry $\vec{R}$. Given an FTQM, the representations of $\hat{H}_{qubit}$ and $|\Psi_{qubit}\rangle$ are detailed in the next section, which serve as the input to quantum algorithms such as VQE and QPE, applicable to both near-term and future fault-tolerant architectures.

2.5 Fermion-to-Qubit Mappings (FTQMs)

Several mapping schemes have been proposed to achieve FTQM efficiently, each balancing trade-offs between operator locality, qubit overhead, and circuit depth[50,52,53,78–85]. In this section, we outline the theoretical background of the three most widely used mappings: JW[50], BK[52], and Pa[53]. For each mapping, we present the corresponding basis construction and show how $(\hat{a}^\dagger, \hat{a})$ are represented in terms of Pauli operators.

2.5.1 Jordan–Wigner (JW)

In the JW mapping, each qubit represents the occupancy of an individual spin orbital, with the computational states $|0\rangle$ and $|1\rangle$ denoting unoccupied and occupied orbitals, respectively[17]. This formulation aligns with the occupation-number basis and is often referred to as the JW basis:

$$|n_{m-1}\rangle \otimes |n_{m-2}\rangle \otimes \ldots \otimes |n_1\rangle \otimes |n_0\rangle \rightarrow |q_{m-1}\rangle \otimes |q_{m-2}\rangle \otimes \cdots \otimes |q_1\rangle \otimes |q_0\rangle, \qquad q_j = f_j \in \{0,1\}. \tag{21}$$

In this representation, the state of each qubit $|q_j\rangle$ encodes the occupation number f_j of the j^{th} spin orbital. The corresponding $(\hat{a}^\dagger, \hat{a})$ in the JW mapping are given by:

$$\hat{a}_j^\dagger \equiv \frac{1}{2}(\hat{\sigma}_x^j - i\hat{\sigma}_y^j) \otimes \hat{\sigma}_{z,\rightarrow}^{j-1}, \qquad \hat{a}_j \equiv \frac{1}{2}(\hat{\sigma}_x^j + i\hat{\sigma}_y^j) \otimes \hat{\sigma}_{z,\rightarrow}^{j-1}, \tag{22}$$

where $\hat{\sigma}_{z,\rightarrow}^j \equiv \hat{\sigma}_z^j \otimes \hat{\sigma}_z^{j-1} \otimes \cdots \otimes \hat{\sigma}_z^1 \otimes \hat{\sigma}_z^0$, and any qubit not explicitly acted upon is implicitly operated on by $\hat{\mathbb{I}}_2$. The operator $\hat{\sigma}_{z,\rightarrow}^{j-1}$ acts as a parity string, with eigenvalues ± 1 corresponding to even or odd parity states, respectively[53].

While conceptually straightforward, the JW transformation introduces long Pauli strings, leading to increased circuit depth for non-local operators. The BK transformation addresses this limitation by balancing parity and occupation information across qubits.

2.5.2 Bravyi–Kitaev (BK)

In the BK transformation, each qubit encodes a partial parity of the fermionic occupation numbers, rather than a single orbital occupation[17]. This results in a more balanced distribution of parity and occupation information across qubits, leading to logarithmic rather than linear operator locality[52]. The occupation numbers contributing to each partial sum are determined by the BK transformation matrix β_m:

$$|n_{m-1}\rangle \otimes |n_{m-2}\rangle \otimes \ldots \otimes |n_1\rangle \otimes |n_0\rangle \rightarrow |q_{m-1}\rangle \otimes |q_{m-2}\rangle \otimes \cdots \otimes |q_1\rangle \otimes |q_0\rangle, \qquad q_j = \left[\sum_{k=0}^{j} [\beta_m]_{jk} f_k\right] \bmod 2. \tag{23}$$

Here, β_m denotes the transformation matrix that maps occupation-number basis vectors of dimension m to their corresponding BK basis representation. The matrix is recursively defined as:

$$\beta_1 = [1], \quad \beta_{2^{l+1}} = \begin{bmatrix} \beta_{2^l} & \alpha_0 \\ \alpha_1 & \beta_{2^l} \end{bmatrix}, \tag{24}$$

In this formulation, α_0 represents a $[2^l \times 2^l]$ zero matrix, while α_1 is also a $[2^l \times 2^l]$ zero matrix except for its bottom row, which is filled with ones. The corresponding $(\hat{a}^\dagger, \hat{a})$ in this mapping are defined as:

$$\hat{a}_j^\dagger \equiv \frac{1}{2}(\hat{\sigma}_x^{U(j)} \otimes \hat{\sigma}_x^j \otimes \hat{\sigma}_z^{P(j)} - i\hat{\sigma}_x^{U(j)} \otimes \hat{\sigma}_y^j \otimes \hat{\sigma}_z^{\rho(j)}); \qquad \hat{a}_j \equiv \frac{1}{2}(\hat{\sigma}_x^{U(j)} \otimes \hat{\sigma}_x^j \otimes \hat{\sigma}_z^{P(j)} + i\hat{\sigma}_x^{U(j)} \otimes \hat{\sigma}_y^j \otimes \hat{\sigma}_z^{\rho(j)}). \tag{25}$$

Where,

$$\rho(j) \equiv \begin{cases} P(j) & \text{if } j \text{ is even;} \\ R(j) & \text{if } j \text{ is odd.} \end{cases} \tag{26}$$

and $R(j) \equiv P(j) \setminus F(j)$, where $R(j)$, $P(j)$, $F(j)$, and $U(j)$ correspond to the remainder, parity, flip, and update sets, respectively[53].

Alternatively, the Parity mapping encodes parity information directly on each qubit, providing symmetry-related benefits and facilitating efficient qubit tapering.

2.5.3 Parity (Pa)

In the Parity mapping, parity information is encoded locally on each qubit, whereas occupation numbers are represented non-locally[17]. The j^{th} qubit thus corresponds to the parity of the first j fermionic modes:

$$|n_{m-1}\rangle \otimes |n_{m-2}\rangle \otimes \ldots \otimes |n_1\rangle \otimes |n_0\rangle \rightarrow |q_{m-1}\rangle \otimes |q_{m-2}\rangle \otimes \cdots \otimes |q_1\rangle \otimes |q_0\rangle, \quad q_j = \left[\sum_{k=0}^{j} [\pi_m]_{jk} f_k\right] \bmod 2 = \left[\sum_{k=0}^{j} f_k\right] \bmod 2, \tag{27}$$

where the associated transformation matrix π_m is defined as:

$$[\pi_m]_{jk} = \begin{cases} 1 & j < k \\ 0 & j \geq k \end{cases}. \tag{28}$$

The $(\hat{a}^\dagger, \hat{a})$ under this mapping are expressed as:

$$\hat{a}_j^\dagger \equiv \frac{1}{2}(\hat{\sigma}_{x,\leftarrow}^{j+1} \otimes \hat{\sigma}_x^j \otimes \hat{\sigma}_z^{j-1} - i\hat{\sigma}_{x,\leftarrow}^{j+1} \otimes \hat{\sigma}_y^j); \qquad \hat{a}_j \equiv \frac{1}{2}(\hat{\sigma}_{x,\leftarrow}^{j+1} \otimes \hat{\sigma}_x^j \otimes \hat{\sigma}_z^{j-1} + i\hat{\sigma}_{x,\leftarrow}^{j+1} \otimes \hat{\sigma}_y^j), \tag{29}$$

here, $\hat{\sigma}^{j}_{x,\leftarrow} \equiv \hat{\sigma}^{m-1}_{x} \otimes \hat{\sigma}^{m-2}_{x} \otimes \cdots \otimes \hat{\sigma}^{j+1}_{x} \otimes \hat{\sigma}^{j}_{x}$ denotes the update operator, responsible for flipping all qubits associated with partial sums that contain the $(j-1)^{\text{th}}$ orbital whenever its occupation state changes[53].

In Pa, when spin-orbitals are ordered in separate spin blocks, and the total particle number (and/or spin sector) is known, it permits an immediate two-qubit reduction by fixing global parity eigenvalues. This two-qubit reduction is a consequence of two independent $\mathbb{Z}_2$ symmetries (particle-number parity and an ordering-induced parity); each fixed symmetry allows removing one qubit by replacing its Pauli operator with its eigenvalue[49,53].

2.6 Hamiltonian Reduction Strategies

Following the transformation of the fermionic Hamiltonian into its qubit representation $\hat{H}_{qubit}$, additional reductions can be applied to optimize computational resources without compromising the physical fidelity of the simulation. Despite efficient FTQMs, the resulting $\hat{H}_{qubit}$ often contains redundant degrees of freedom that exceed the capabilities of current NISQ and near-term devices. To address this, reduction techniques are used to minimize the active qubit space and simplify the operator structure while preserving the eigenvalue spectrum relevant to the target state.

2.6.1 Frozen-Core Approximation

The frozen-core (FC) approximation leverages the observation that core orbitals that are deeply bound and chemically inert contribute negligibly to correlation effects among valence electrons. These orbitals are treated as doubly occupied and excluded from the active orbital space used in electronic correlation and qubit mapping[86,87], yielding an FC Hamiltonian $\hat{H}_{fc}$:

$$\hat{H}_{fc} = E_{core} + \sum_{pq}^{active} h_{pq}\,\hat{a}^{\dagger}_{p}\hat{a}_{q} + \frac{1}{2}\sum_{pqrs}^{active} h_{pqrs}\,\hat{a}^{\dagger}_{p}\hat{a}^{\dagger}_{q}\hat{a}_{r}\hat{a}_{s}, \tag{30}$$

where E_{core} is the energy contribution from the frozen orbitals, and the summations are restricted to the active orbital subset. This approach substantially reduces the number of qubits, one- and two-electron terms, while maintaining chemical accuracy for valence properties[48].

2.6.2 $\mathbb{Z}_2$ Symmetry Tapering

Many fermionic Hamiltonians possess discrete symmetries that form an Abelian $\mathbb{Z}_2$ group[49,88]. Each independent generator corresponds to a conserved quantum number, such as particle-number parity, total spin-parity, or molecular point-group symmetry, and partitions the Hilbert space into distinct symmetry sectors.

The $\mathbb{Z}_2$ symmetry converter identifies these commuting symmetries from the qubit Hamiltonian and exploits them to remove redundant qubits. For each symmetry generator with a known eigenvalue ± 1, one qubit can be eliminated, yielding a reduced Hamiltonian:

$$\hat{H}_{tapered} = \mathscr{T}(\hat{H}_{qubit}), \tag{31}$$

where $\mathscr{T}$ embeds the symmetry constraints into the remaining qubits. This process preserves the physical spectrum while significantly reducing qubit count and circuit depth[49,89]. Formally, the tapering procedure identifies an Abelian subgroup $\mathscr{S} \subset \mathscr{P}_N$ of the N-qubit Pauli group:

$$\mathscr{P}_N = \pm\{\hat{\mathbb{I}}_2, \hat{\sigma}_x, \hat{\sigma}_y, \hat{\sigma}_z\}^{\otimes N}, \tag{32}$$

such that all $\hat{s} \in \mathscr{S}$ commute with $\hat{H}_{qubit}$. Each $\hat{s}_j$ defines a $\mathbb{Z}_2$ symmetry with eigenvalues ± 1. Clifford transformations $\hat{U}_j$ map these generators to single-qubit Pauli operators:

$$\hat{U}_j \hat{s}_j \hat{U}_j^{\dagger} = \sigma_x^{(q_j)}, \tag{33}$$

allowing qubits q_j to be replaced by their eigenvalues and removed from the simulation[89]. Beyond $\mathbb{Z}_2$ symmetries, additional reductions based on spatial geometry, like point-group symmetries, can be combined with tapering for further compression of the active Hilbert space[49,89,90].

Together, the FC approximation and $\mathbb{Z}_2$ tapering represent two complementary reduction techniques that, when combined with efficient FTQMs, enable scalable quantum algorithms for molecular simulations within the resource limits of NISQ and near-term quantum hardware[20]. Building on these theoretical foundations, the following section outlines the quantitative methodology employed to evaluate these strategies and their associated resource trade-offs.

3 Methodology

The overall methodology for performing resource estimation in VQE-based molecular simulations is divided into four sequential stages, as summarized below. Each stage transforms the molecular input into progressively more universal gate-based QC hardware-relevant representations, culminating in circuit-level resource metrics.

The molecular geometry (in Cartesian coordinates), basis set, total spin, charge, and the desired backend are taken as input for resource estimation. The process is divided into four sequential stages: Hamiltonian Modeling, Qubit Mapping, Ansatz Preparation, and Quantum Circuit Preparation, each producing specific intermediate and final outputs, as shown in Figure 2.

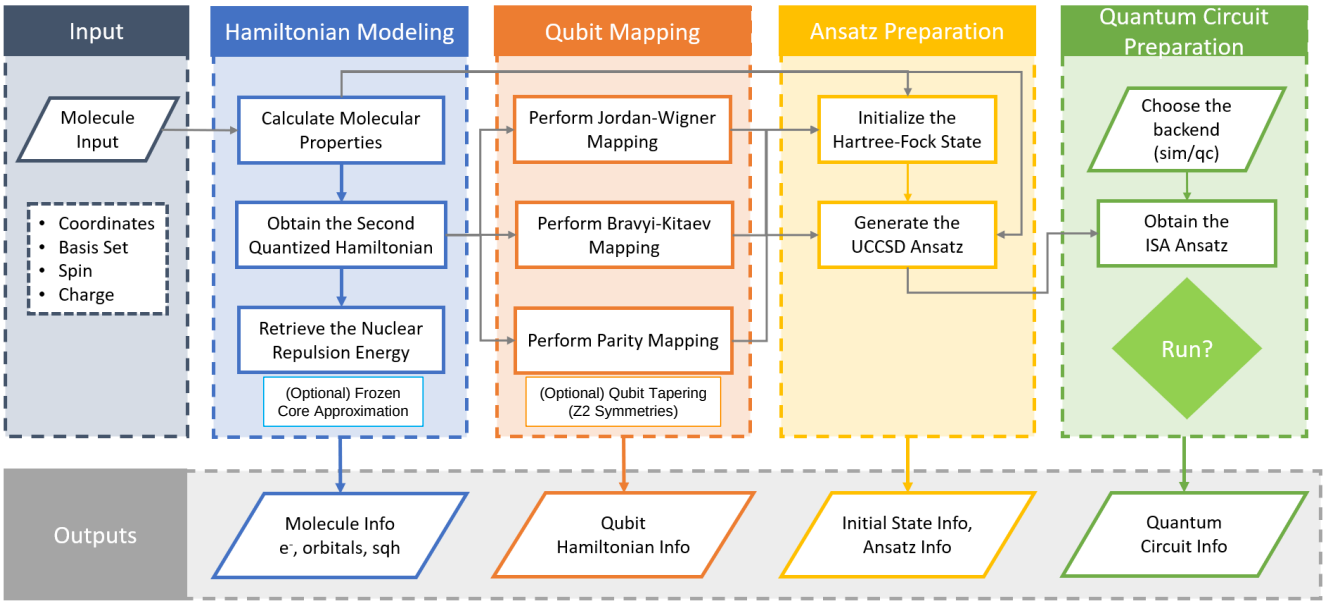

Figure 2. Workflow for resource estimation in the VQE framework, showing the sequence from molecular input to Hamiltonian modeling, qubit mapping, ansatz construction, and circuit compilation, along with key outputs at each stage.

3.1 Hamiltonian Modeling

In this stage, molecular properties are computed using the chosen basis set, and the second-quantized electronic Hamiltonian $\hat{H}_{sq}$ is obtained. The nuclear–nuclear repulsion energy term, $\hat{V}_{NN}$, is also retrieved. Hamiltonian reduction may be performed by enabling the frozen-core approximation, which decreases the number of active orbitals and thereby reduces both qubit requirements and gate counts. The outputs of this stage include the number of α and β electrons, the number of spatial and spin orbitals, $\hat{V}_{NN}$, and the $\hat{H}_{sq}$.

3.2 Qubit Mapping

The $\hat{H}_{sq}$ is transformed into its qubit-representable form, $\hat{H}_{qubit}$, through FTQMs such as JW, BK, and Pa. To further reduce the Hamiltonian dimension, qubit tapering via $\mathbb{Z}_2$ symmetries can be applied, lowering the qubit count without introducing approximation. The outputs of this stage include the $\hat{H}_{qubit}$, the total number of Pauli strings, and their decomposition into $\hat{\sigma}_x$, $\hat{\sigma}_y$, $\hat{\sigma}_z$, and $\hat{\mathbb{I}}_2$ operators.

3.3 Ansatz Preparation

The Hartree-Fock[91] reference state $|\psi_{HF}\rangle$ is formulated using molecular parameters derived from the Hamiltonian modeling stage. Subsequently, the UCCSD ansatz is constructed to approximate the molecular ground state within the defined active space. The resulting outputs comprise detailed specifications of the initial state and the parametrized UCCSD ansatz corresponding to the target molecule.

3.4 Quantum Circuit Preparation

In the final stage, the UCCSD ansatz is compiled into the Instruction Set Architecture (ISA) format for a designated quantum simulator or hardware backend. This yields circuit-level resource information, including the number of qubits, total quantum gates, circuit depth, single-qubit and two-qubit gate counts, and individual gate breakdowns by type.

Together, these stages provide a comprehensive framework for assessing the computational resources required to simulate a given molecular system on a specific quantum simulator/hardware backend. The implementation was carried out in `Python (v3.11)`[92,93] using `NumPy (v2.2.1)`[94], `PySCF (v2.7.0)`[95–97], `Qiskit (v1.3.1)`[98], `Qiskit-Aer (v0.15.1)`[98,99], and `Qiskit-Nature (v0.7.2)`[100]. The results obtained from this workflow for the representative set of molecular systems are discussed in the following section.

4 Results and Discussion

We first present the results obtained from VQE(UCCSD)-based resource estimation performed using the workflow described in Section 3 on two representative molecular systems: Methane (CH_4) and Fluoromethane (CH_3F). Their 3-dimensional (3D) molecular geometries are shown in Figure 3, and the corresponding atomic coordinates are provided in Table S1 of the Supplementary Information. Both geometries were generated using the `Avogadro` molecular editor[101] using its built-in universal force field (UFF) auto-optimisation tool[102]. These molecules are employed here as input geometries for the purpose of illustrating the resource-estimation workflow.

For a direct comparison, all calculations employed the same STO-3G basis set and the JW FTQM, without applying any Hamiltonian reduction techniques mentioned in Section 2.6. The ISA-level ansatz circuits were transpiled using optimization level 3 and the `Qiskit-Aer` simulator backend in `Qiskit`. The simulator was employed with its default transpilation configuration, corresponding to an all-to-all qubit connectivity model without a hardware-imposed coupling map. As a result, no initial layout selection or routing procedures were required. Circuits were decomposed into the default transpilation target gate set of the `Qiskit-Aer` backend, consisting of single-qubit gates $\{\mathrm{U}_2(\phi,\lambda), \mathrm{R}_Z(\theta), \mathrm{R}_Y(\theta), \mathrm{H}, \mathrm{S}_X\ (\sqrt{X}), \mathrm{S}_X\mathrm{dg}\ (\sqrt{X}^\dagger), \mathrm{X}\}$ and two-qubit gates {CX, `UnitaryGate`[103]}. Under these conditions, the transpilation process is deterministic and yields identical compiled circuits across repeated runs for a given input circuit. The same compilation configuration was consistently applied to all subsequent calculations presented in this work.

Table 1 summarizes the results from the Hamiltonian Modeling and Qubit Mapping stages. The outputs include the chosen basis set, number of α and β electrons, number of molecular spatial and spin orbitals (N_{so}), and the $\hat{V}_{NN}$. Additionally, we report the total number of terms in $\hat{H}_{sq}$ (N_{sqh}), the number of Pauli strings in the $\hat{H}_{qubit}$ (N_{PS}), and the respective counts of $\hat{\sigma}_x$, $\hat{\sigma}_y$, $\hat{\sigma}_z$, and $\hat{\mathbb{I}}_2$ (N_X, N_Y, N_Z, N_I). These metrics collectively characterize the algebraic complexity and qubit-space dimensionality of each system. Subsequently, Table 2 presents the results from the Ansatz Preparation and Quantum Circuit Preparation stages. The outputs include the total number of qubits or circuit width (W), variational parameters (P), circuit depth (D), and total quantum gates (G), followed by a breakdown of the quantum gates into single-qubit, two-qubit, and arbitrary gate categories. These results characterize the relevant hardware-agnostic quantum circuit-level resource footprint for executing VQE(UCCSD).

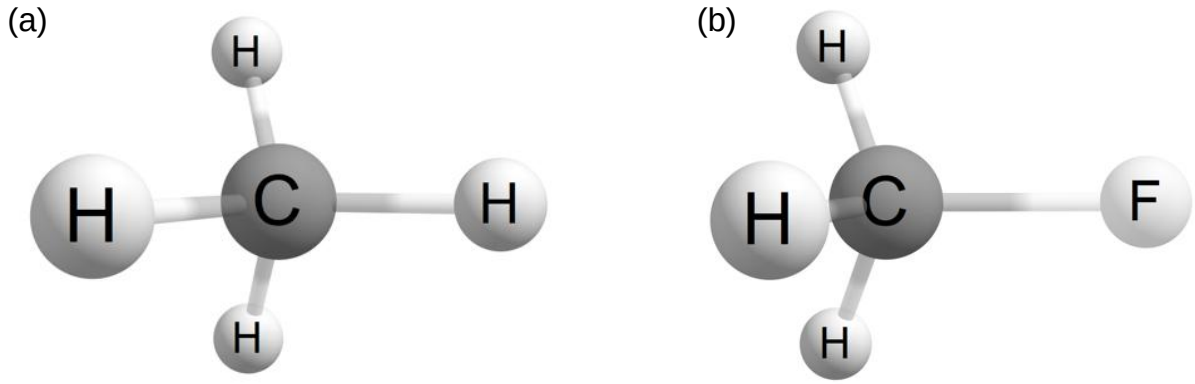

Figure 3. 3D molecular structures: (a) Methane (CH_4) and (b) Fluoromethane (CH_3F).

To further evaluate scalability, we extended our analysis across a series of molecules of increasing electronic and structural complexity, including H_2, LiH, HF, BeH_2, H_2O, N_2, O_2, CO, NH_3, CH_4, C_2H_2, H_2O_2, and C_2H_4, in the STO-3G basis set. For each molecule, the input geometry was obtained by performing a full geometry optimisation at the CCSD/STO-3G level of theory using `PySCF` quantum chemistry package[97]. All optimised atomic coordinates are tabulated in Table S2 of the Supplementary Information. For each molecule, resource estimation was performed under four configurations combining Hamiltonian reduction

Table 1. Resource estimation results for CH_4 and CH_3F. Section 1 of the table presents the molecular information, followed by the $\hat{H}_{sq}$ information in Section 2, and finally the $\hat{H}_{qubit}$ information in Section 3. In Section 1, $\hat{V}_{NN}$ denotes the nuclear–nuclear repulsion energy, as given in Eq. (7); Ha denotes Hartree, and e^- represents an electron. In Section 2, the Number of Terms refers to the number of one- and two-body operators in $\hat{H}_{sq}$, as shown in Eq. (10). In Section 3, the Number of Pauli Strings N_{PS} denotes the unique Pauli strings that compose $\hat{H}_{qubit}$, and the counts of $\hat{\sigma}_x$, $\hat{\sigma}_y$, and $\hat{\sigma}_z$ (N_X, N_Y, N_Z, N_I) indicate the total number of the corresponding Pauli operators appearing across all Pauli strings in $\hat{H}_{qubit}$, as given by Eq. (18).

Property	**Methane (CH_4)**	**Fluoromethane (CH_3F)**
1. Molecular Information		
Basis-Set	STO-3G	STO-3G
Number of α electrons (e^-)	5	9
Number of β electrons (e^-)	5	9
Number of Spatial Orbitals	9	13
Number of Spin Orbitals (N_{so})	18	26
$\hat{V}_{NN}$ in Ha	13.408333940368452	37.83061899847712
2. Second-Quantized Hamiltonian $\hat{H}_{sq}$ Information		
Number of Terms (N_{sqh})	25,350	98,002
3. Qubit Hamiltonian $\hat{H}_{qubit}$ Information		
Number of Pauli Strings (N_{PS})	8,172	28,984
Number of $\hat{\sigma}_x$ [%] (N_X)	13,744 [09.34%]	50,648 [06.72%]
Number of $\hat{\sigma}_y$ [%] (N_Y)	13,744 [09.34%]	50,648 [06.72%]
Number of $\hat{\sigma}_z$ [%](N_Z)	30,612 [20.81%]	166,260 [22.06%]
Number of $\hat{\mathbb{I}}_2$ [%] (N_I)	88,996 [60.50%]	486,028 (64.50%]

Table 2. Resource estimation results for CH_4 and CH_3F. Section 1 of the table provides the ansatz information, while Section 2 presents the quantum circuit information, followed by Sections 2.1, 2.2, and 2.3, which give detailed information on the corresponding single-qubit, two-qubit, and arbitrary gates, respectively. The quantum gate decomposition shown in Section 2 corresponds to using `Qiskit-Aer` as the backend with transpilation optimization level 3 in `Qiskit`. Additional quantum gate information can be found in the Qiskit documentation[104].

Property / Gate	**Methane (CH_4)**	**Fluoromethane (CH_3F)**
1. Ansatz Information		
No. of Qubits (W)	18	26
No. of Parameters (P)	560	1,800
2. Quantum Circuit Information		
Circuit Depth (D)	70,182	3,12,660
Total Gates (G)	77,787	3,37,423
Single-Qubit Gates	12,673	41,985
Two-Qubit Gates	62,468	2,86,892
Arbitrary Gates	2,646	8,546
2.1. Single-Qubit Gates Information		
$\text{U}_2(\phi,\lambda)$	7,339	24,475
$\text{R}_Z(\theta)$	4,240	13,968
H	529	1,733
S_X or $\sqrt{X}$	462	1,518
S_Xdg or $\sqrt{X}^\dagger$	95	275
X	8	16
2.2. Two-Qubit Gates Information		
CX / CNOT	62,468	2,86,892
2.3. Arbitrary-Qubit Gates Information		
Unitary	2,646	8,546

options: frozen-core approximation (F) and $\mathbb{Z}_2$ symmetries, qubit tapering (T), with boolean combinations of:

$$(\mathrm{F},\mathrm{T}) \rightarrow (False, False), (True, False), (False, True), (True, True).$$

Each configuration was evaluated using the JW, BK, and Pa FTQMs, and all circuits were transpiled at optimization level 3 for the `Qiskit-Aer` simulator backend under the same compilation settings described above. The corresponding Hamiltonian and circuit-level resource counts for all configurations are reported in Tables S3 and S4.

In the trivial case of H_2, where no core orbitals are available for freezing, $\mathbb{Z}_2$ tapering effectively reduces the original four-qubit $\hat{H}_{qubit}$ to a single-qubit representation, illustrating the maximum achievable simplification. A structurally informative pattern emerges when examining the width reduction for the systems under study, as shown in Table 3. The underlying raw values from which these reduction factors are computed are listed in Table S4, with the corresponding reduction ratios provided in Table S5. The JW and BK mappers yield identical qubit reductions across all molecules and all configurations. This equivalence arises as both encodings preserve the full N-qubit active space before any symmetry reduction, meaning the number of qubits that can be eliminated through tapering or the frozen-core approximation is governed entirely by the molecular symmetry content rather than the choice of mapping. The Pa mapper, in contrast, provides a default two-qubit overhead saving. This reduction stems from two independent $\mathbb{Z}_2$ symmetries, whose fixed eigenvalues allow two qubits to be removed at the encoding level, as detailed in Section 2.5. However, because these symmetries are already incorporated into the encoding, the number of additional exploitable $\mathbb{Z}_2$ symmetries available for post-mapping tapering is reduced or eliminated[49]. Specifically, for NH_3, CH_4, C_2H_2, and H_2O_2, the Pa mapper under the tapering-only (T) configuration yields no further width reduction, as confirmed by the 0.0% entries in Table 3. We note that this interaction between the intrinsic symmetry capacity of the mapper and the molecule's symmetry content constitutes an important constraint that practitioners should consider when selecting a mapping strategy.

Table 3. Circuit width reduction (in %) relative to the no-tapering, no-frozen-core baseline (-) for each molecule, qubit mapper, and reduction strategy combination. Reduction percentage is computed as $100 \times (Q_{-} - Q_{\text{combo}})/Q_{-}$, where Q denotes the total qubit count. A value of x% indicates that the optimised circuit requires x% fewer qubits than the baseline. T = tapering only; F = frozen core only; TF = both tapering and frozen core applied. Summary statistics (min, max, mean, median) are computed across all 12 molecules per column.

	Jordan–Wigner			**Bravyi–Kitaev**			**Parity**		
Molecule	**T**	**F**	**TF**	**T**	**F**	**TF**	**T**	**F**	**TF**
LiH	33.3%	16.7%	50.0%	33.3%	16.7%	50.0%	20.0%	20.0%	40.0%
HF	33.3%	16.7%	50.0%	33.3%	16.7%	50.0%	20.0%	20.0%	40.0%
BeH_2	35.7%	14.3%	50.0%	35.7%	14.3%	50.0%	25.0%	16.7%	41.7%
H_2O	21.4%	14.3%	35.7%	21.4%	14.3%	35.7%	8.3%	16.7%	25.0%
NH_3	12.5%	12.5%	25.0%	12.5%	12.5%	25.0%	0.0%	14.3%	14.3%
CH_4	11.1%	11.1%	22.2%	11.1%	11.1%	22.2%	0.0%	12.5%	12.5%
O_2	25.0%	20.0%	45.0%	25.0%	20.0%	45.0%	16.7%	22.2%	38.9%
N_2	20.0%	20.0%	40.0%	20.0%	20.0%	40.0%	11.1%	22.2%	33.3%
CO	15.0%	20.0%	35.0%	15.0%	20.0%	35.0%	5.6%	22.2%	27.8%
C_2H_2	8.3%	16.7%	25.0%	8.3%	16.7%	25.0%	0.0%	18.2%	18.2%
H_2O_2	8.3%	16.7%	25.0%	8.3%	16.7%	25.0%	0.0%	18.2%	18.2%
C_2H_4	10.7%	14.3%	25.0%	10.7%	14.3%	25.0%	3.8%	15.4%	19.2%
Min	8.3%	11.1%	22.2%	8.3%	11.1%	22.2%	0.0%	12.5%	12.5%
Max	35.7%	20.0%	50.0%	35.7%	20.0%	50.0%	25.0%	22.2%	41.7%
Mean	19.6%	16.1%	35.7%	19.6%	16.1%	35.7%	9.2%	18.2%	27.4%
Median	17.5%	16.7%	35.4%	17.5%	16.7%	35.4%	7.0%	18.2%	26.4%

Beyond H_2, for the given set of molecules, tapering and frozen-core techniques yield progressively smaller reductions but still significantly lower the total gate count and qubit width, as shown in Figure 4. A finer-grained inspection of the qubit widths, reported in Table 3, reveals that the frozen-core approximation (F) delivers more uniform width reductions across molecules. This reduction ranges from 11.1% to 20.0% for JW and BK, whereas tapering alone (T) exhibits considerably higher variance, spanning from 0% to 35.7% depending on the available $\mathbb{Z}_2$ symmetries of the system. This uniformity is physically intuitive: freezing core orbitals removes a fixed number of spin-orbitals proportional to the number of inner-shell electrons, which scales predictably with atomic composition, whereas tapering is highly sensitive to point-group symmetry and may yield no benefit when the applicable symmetry sectors are already saturated. When both techniques are combined (TF),

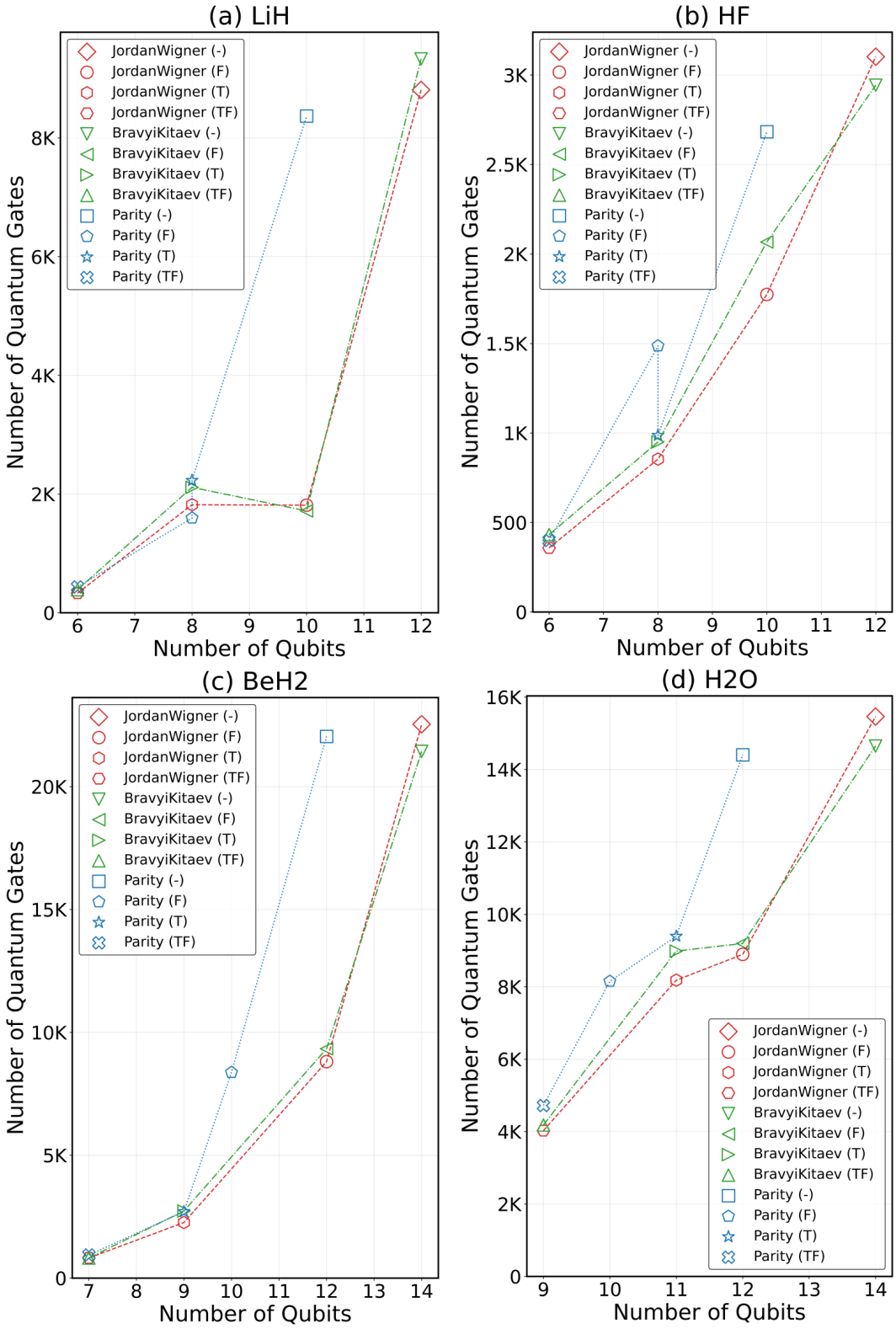

Figure 4. Scaling behaviour of qubit and gate requirements across molecular systems using JW, BK, Pa mappings and Hamiltonian reduction configurations. (a)-(d) correspond to the first set of molecular systems (LiH, HF, BeH_2, and H_2O). Here, T denotes qubit tapering via $\mathbb{Z}_2$ symmetries, and F denotes the FC approximation. Symbols indicate the applied configurations: (–) both T and F are false, (T) only tapering is applied, (F) only frozen-core is applied, and (TF) both techniques are applied. Error bars are omitted as the resource-estimation procedure is deterministic.

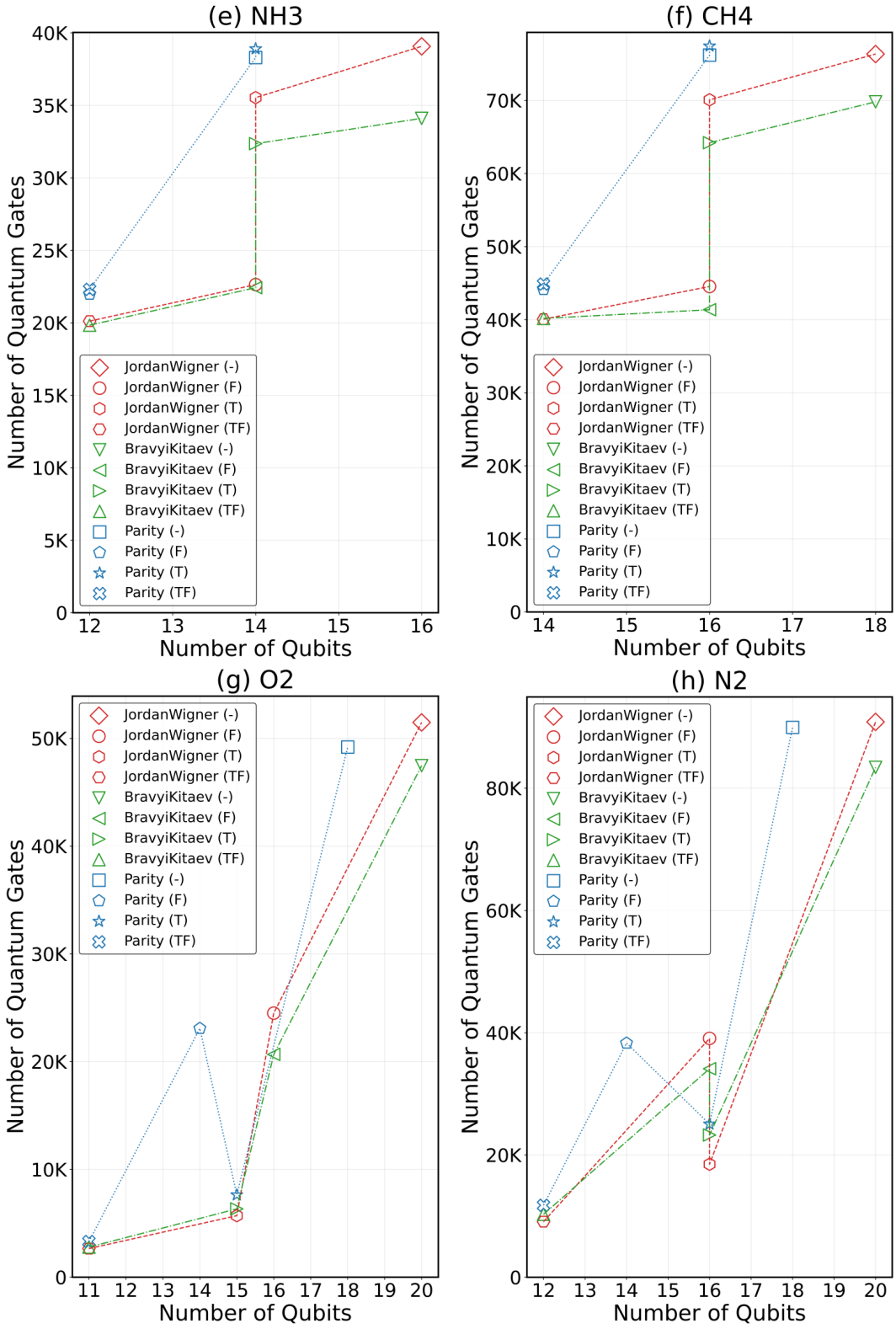

Figure 4. (continued) Scaling behaviour of qubit and gate requirements across molecular systems using JW, BK, Pa mappings and Hamiltonian reduction configurations. (e)-(h) correspond to the next set of molecular systems ($NH_3, CH_4, O_2,$ and N_2). Here, T denotes qubit tapering via $\mathbb{Z}_2$ symmetries, and F denotes the FC approximation. Symbols indicate the applied configurations: (–) both T and F are false, (T) only tapering is applied, (F) only frozen-core is applied, and (TF) both techniques are applied. Error bars are omitted as the resource-estimation procedure is deterministic.

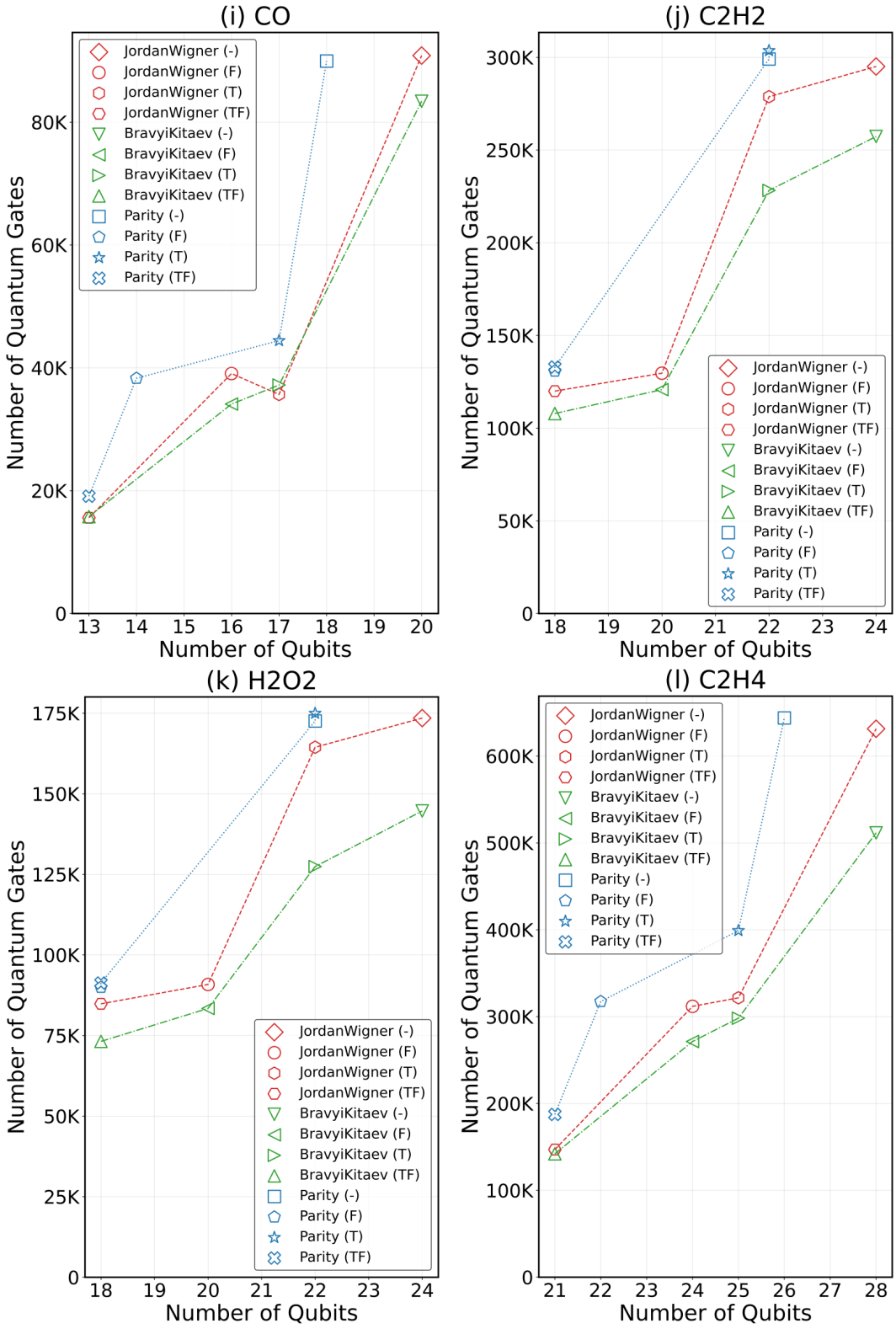

Figure 4. (continued) Scaling behaviour of qubit and gate requirements across molecular systems using JW, BK, Pa mappings and Hamiltonian reduction configurations. (i)-(l) correspond to the remaining molecular systems (CO, C_2H_2, H_2O_2, and C_2H_4). Here, T denotes qubit tapering via $\mathbb{Z}_2$ symmetries, and F denotes the FC approximation. Symbols indicate the applied configurations: (–) both T and F are false, (T) only tapering is applied, (F) only frozen-core is applied, and (TF) both techniques are applied. Error bars are omitted as the resource-estimation procedure is deterministic.

the reductions compound, with the mean width reduction rising to 35.7% for JW and BK and 27.4% for the Pa mapper, as summarized in the statistical rows of Table 3.

Complementing the qubit-width analysis, it is informative to examine how the Hamiltonian-level operator count, specifically the number of unique Pauli strings N_{PS} in $\hat{H}_{\mathrm{qubit}}$, responds to the same reduction strategies. This quantity is directly relevant to the measurement cost of VQE, since each unique Pauli string in $\hat{H}_{\mathrm{qubit}}$ in principle requires a separate measurement circuit when evaluating expectation values, and the total number of measurements scales with both N_{PS} and the statistical precision required[32,33]. The corresponding reduction factors for N_{PS} across all molecules, mappers, and configurations are summarised in Table 4. A structurally significant observation is that N_{PS} reduction factors are identical across all three mappers for every molecule and configuration. This mapper independence arises as the count of unique Pauli strings is determined by the molecular symmetry and active-space structure rather than the specific FTQM, which affects the form of individual strings but not their total number. Consequently, it may be inferred that the choice of mapper has no bearing on measurement cost as quantified by N_{PS}.

In terms of the magnitude of reduction, the frozen-core approximation (F) and its combination with symmetry tapering (TF) deliver the most meaningful N_{PS} compression, with mean reduction factors of 2.09× and 2.21×, respectively, and peak values reaching 2.71× for O_2 (F) and 2.75× for O_2 (TF). By contrast, tapering alone (T) yields negligible N_{PS} reduction for most molecules, with a mean of 1.03× and a median of 1.00×, confirming that $\mathbb{Z}_2$ symmetry tapering primarily reduces the number of qubits and simplifies operator weights rather than eliminating large numbers of unique measurement bases. The notable exception is H_2, where the absence of core orbitals precludes the frozen-core approximation entirely, and the high point-group symmetry of the system allows tapering alone to reduce N_{PS} from 15 to 3, a 5× compression that reflects the maximum symmetry exploitation achievable for this well-studied two-electron system[20,23]; H_2 is accordingly excluded from the 12-molecule summary statistics reported here. For molecules such as NH_3, CH_4, O_2, N_2, CO, C_2H_2, H_2O_2, and C_2H_4, the tapering-only (T) reduction factor is exactly 1.00×, meaning that N_{PS} is entirely unchanged by symmetry tapering alone. These findings indicate that the frozen-core approximation is the dominant mechanism for reducing measurement overhead among the strategies examined here, and that its effect compounds only modestly when combined with tapering. It should be noted that this study focuses on circuit-level resource requirements, and a full quantitative analysis of measurement cost, including shot-count estimation and Pauli grouping strategies, is outside the scope of the present work and is deferred as a natural direction for future investigation.

Table 4. Pauli string count (N_{PS}) reduction factor relative to the no-tapering, no-frozen-core baseline (-) for each molecule, qubit mapper, and reduction strategy combination. Reduction factor is computed as $N_{\mathrm{PS},-}/N_{\mathrm{PS,combo}}$, where N_{PS} denotes the number of unique Pauli strings in the qubit Hamiltonian $\hat{H}_{\mathrm{qubit}}$. A value of $k\times$ indicates the optimised Hamiltonian contains k times fewer Pauli strings than the baseline. T = tapering only; F = frozen core only; TF = both tapering and frozen core applied. Summary statistics (min, max, mean, median) are computed across all 12 molecules per column.

	Jordan–Wigner			**Bravyi–Kitaev**			**Parity**		
Molecule	**T**	**F**	**TF**	**T**	**F**	**TF**	**T**	**F**	**TF**
LiH	1.13×	2.29×	2.73×	1.13×	2.29×	2.73×	1.13×	2.29×	2.73×
HF	1.13×	2.29×	2.73×	1.13×	2.29×	2.73×	1.13×	2.29×	2.73×
BeH_2	1.12×	2.04×	2.49×	1.12×	2.04×	2.49×	1.12×	2.04×	2.49×
H_2O	1.04×	1.97×	2.08×	1.04×	1.97×	2.08×	1.04×	1.97×	2.08×
NH_3	1.00×	1.55×	1.55×	1.00×	1.55×	1.55×	1.00×	1.55×	1.55×
CH_4	1.00×	1.47×	1.47×	1.00×	1.47×	1.47×	1.00×	1.47×	1.47×
O_2	1.00×	2.71×	2.75×	1.00×	2.71×	2.75×	1.00×	2.71×	2.75×
N_2	1.00×	2.51×	2.51×	1.00×	2.51×	2.51×	1.00×	2.51×	2.51×
CO	1.00×	2.50×	2.50×	1.00×	2.50×	2.50×	1.00×	2.50×	2.50×
C_2H_2	1.00×	2.02×	2.02×	1.00×	2.02×	2.02×	1.00×	2.02×	2.02×
H_2O_2	1.00×	1.93×	1.93×	1.00×	1.93×	1.93×	1.00×	1.93×	1.93×
C_2H_4	1.00×	1.76×	1.77×	1.00×	1.76×	1.77×	1.00×	1.76×	1.77×
Min	1.00×	1.47×	1.47×	1.00×	1.47×	1.47×	1.00×	1.47×	1.47×
Max	1.13×	2.71×	2.75×	1.13×	2.71×	2.75×	1.13×	2.71×	2.75×
Mean	1.03×	2.09×	2.21×	1.03×	2.09×	2.21×	1.03×	2.09×	2.21×
Median	1.00×	2.03×	2.29×	1.00×	2.03×	2.29×	1.00×	2.03×	2.29×

Turning to the number of quantum gates, the impact on total gate counts is more heterogeneous across the molecular set. As detailed in Table 5, when both symmetry tapering and the frozen-core approximation are applied, the JW mapping exhibits

reductions ranging from 1.91× for CH_4 to 27.48× for BeH_2, with a mean of 9.55× and a median of 5.06×. The pronounced separation between the mean and median indicates that a small subset of molecules, principally BeH_2, LiH, and O_2, benefit disproportionately from favourable symmetry structure and a comparatively large frozen-core contribution. The complete set of reduction factors for all resource metrics is provided in Table S5. For the majority of molecules in the benchmark set, the gate reduction clusters more modestly around 2× to 5× under the combined application of both techniques. It should be noted that this variability has practical implications, as aggregate resource savings inferred from a limited number of highly symmetric molecular systems may overestimate the reductions achievable for a representative workload. Therefore, careful, system-specific resource estimation is warranted.

Table 5. Total gate count reduction factor ($N_\times$) relative to the no-tapering, no-frozen-core baseline (-) for each molecule, qubit mapper, and reduction strategy combination. Reduction factor is computed as G_- / G_{combo}, where G denotes the total gate count. A value of $k\times$ indicates the optimised circuit requires k times fewer gates than the baseline. Values below 1.00× indicate a marginal gate count increase versus baseline. T = tapering only; F = frozen core only; TF = both tapering and frozen core applied. Summary statistics (min, max, mean, median) are computed across all 12 molecules per column.

	Jordan–Wigner			**Bravyi–Kitaev**			**Parity**		
Molecule	**T**	**F**	**TF**	**T**	**F**	**TF**	**T**	**F**	**TF**
LiH	4.84×	4.86×	26.69×	4.42×	5.44×	24.05×	3.75×	5.24×	19.24×
HF	3.63×	1.75×	8.66×	3.10×	1.42×	6.81×	2.72×	1.80×	6.71×
BeH_2	9.96×	2.56×	27.48×	7.85×	2.30×	26.17×	8.15×	2.63×	23.42×
H_2O	1.89×	1.74×	3.84×	1.63×	1.59×	3.50×	1.53×	1.77×	3.05×
NH_3	1.10×	1.73×	1.94×	1.05×	1.52×	1.72×	0.98×	1.74×	1.72×
CH_4	1.09×	1.71×	1.91×	1.09×	1.69×	1.74×	0.98×	1.73×	1.70×
O_2	9.02×	2.10×	19.42×	7.49×	2.30×	17.02×	6.44×	2.13×	14.88×
N_2	4.92×	2.33×	9.99×	3.59×	2.45×	8.10×	3.59×	2.35×	7.64×
CO	2.55×	2.33×	5.83×	2.24×	2.45×	5.29×	2.02×	2.35×	4.71×
C_2H_2	1.06×	2.28×	2.46×	1.13×	2.13×	2.39×	0.99×	2.29×	2.25×
H_2O_2	1.06×	1.91×	2.05×	1.14×	1.73×	1.98×	0.99×	1.92×	1.89×
C_2H_4	1.96×	2.02×	4.30×	1.72×	1.89×	3.60×	1.61×	2.03×	3.44×
Min	1.06×	1.71×	1.91×	1.05×	1.42×	1.72×	0.98×	1.73×	1.70×
Max	9.96×	4.86×	27.48×	7.85×	5.44×	26.17×	8.15×	5.24×	23.42×
Mean	3.59×	2.28×	9.55×	3.04×	2.24×	8.53×	2.81×	2.33×	7.55×
Median	2.25×	2.06×	5.06×	1.98×	2.01×	4.45×	1.81×	2.08×	4.08×

The results indicate that although the JW mapping provides the most straightforward implementation, the BK mapping can yield superior compactness in specific cases. For larger molecules such as CO, C_2H_2, H_2O_2, and C_2H_4, the BK mapping tends to produce shallower circuits with fewer total gates, as illustrated in Figure 4. The relative positioning of these three mappers can be further clarified by examining their statistical summary, as presented in Table 5. Across all molecules, the JW mapper achieves the highest mean gate reduction when both tapering and frozen-core approximation are applied (9.55×), followed by BK (8.53×) and Pa (7.55×). The ordering is reversed and compressed when only the frozen-core approximation is applied, with all three mappers statistically near-equivalent (means of 2.28×, 2.24×, and 2.33×, respectively), suggesting that the frozen-core approximation alone is largely mapper-agnostic in its effect. The largest absolute spread between mappers emerges when only symmetry tapering is applied, where JW's mean of 3.59× substantially exceeds Pa's 2.81×, reinforcing the observation that $\mathbb{Z}_2$ tapering interacts most favourably with the JW encoding.

A more consequential observation emerges for the Pa mapper under tapering-only configurations, where a marginal gate-count increase relative to the unoptimised baseline is observed for NH_3, CH_4, C_2H_2, and H_2O_2, with reduction factors of approximately 0.98× to 0.99×, as shown in Table 5. The full reduction data for these cases are reported in Table S5. This counterintuitive outcome arises because the parity encoding redistributes fermionic occupation information into cumulative parity operators, which can increase the entangling structure of the resulting Pauli strings. When this increase is not offset by a sufficient reduction in operator count from tapering, a net gate overhead may result. Importantly, the frozen-core approximation restores the benefit for these molecules: both the frozen-core approximation alone and its combination with symmetry tapering yield positive reductions across all molecules and all mappers, as confirmed by the absence of sub-unity entries in the corresponding columns of Table 5. It may therefore be inferred that this finding provides a practical guideline: when employing the Pa mapper, the frozen-core approximation should be applied as a minimum prerequisite to ensure that symmetry-based optimisations do not inadvertently increase circuit costs.

Finally, it is worth noting that the relationship between qubit count and total gate count is not linear across the molecule set, as shown in Figure 4. Molecules such as BeH_2 and O_2, despite having comparable qubit counts to LiH and HF after both symmetry tapering and frozen-core approximations are applied, exhibit markedly different absolute gate counts. This non-linearity reflects the sensitivity of gate complexity to operator density in the qubit Hamiltonian, a property governed by molecular symmetry and orbital structure.

These trends suggest a practical hierarchy to guide informed FTQM selection and compilation strategies for near-term molecular VQE-UCCSD experiments: for systems where only tapering is feasible, JW or BK should be favoured; where the frozen-core approximation is available, all three mappers are broadly competitive; and where both reductions are applicable, JW and BK deliver the greatest aggregate gate savings, with BK providing an additional advantage in total number of quantum gates for the larger molecules as noted previously in this study.

5 Conclusion

This work presents a systematic framework for hardware-agnostic quantum resource estimation in molecular simulations based on VQE using the UCCSD ansatz. By integrating Hamiltonian modeling, qubit mapping, ansatz construction, and circuit compilation within a unified workflow, we provide an end-to-end assessment of the general computational requirements for executing chemistry-relevant problems on NISQ and near-term quantum hardware, with the physical circuit-level metrics reported here serving as a reference baseline for future logical-resource analyses targeting fault-tolerant quantum systems. Our results demonstrate that FTQMs and Hamiltonian reduction strategies significantly affect quantum circuit complexity. Techniques such as frozen-core approximation and $\mathbb{Z}_2$ symmetry tapering can substantially lower qubit counts and quantum gate operations without sacrificing physical accuracy. The scaling analysis across the benchmarked molecular systems quantitatively establishes that optimal combinations of mapping and reduction can reduce total qubits by up to $\approx 50\%$, Pauli string counts by up to $\approx 2.75\times$ and quantum gates by up to $\approx 27.5\times$, compared to the unreduced Hamiltonian under identical active-space and compilation settings, thereby improving the feasibility of molecular simulations on NISQ and near-term quantum hardware.

A natural extension of this work is the systematic integration of other FTQMs, particularly those based on ternary-tree constructions, into the resource estimation pipeline. Recent advances, such as optimal tree mappings[79], compact and hierarchical encodings[80,81], ultrafast hybrid mappings[82], and physically inspired low-entanglement schemes[83], have demonstrated significant reductions in both qubit overhead and Pauli operator weight compared to canonical JW and BK mappings. Incorporating, benchmarking, and cross-comparing these mappings within our unified workflow would enable a more precise characterization of mapping-ansatz-hardware co-dependencies. In particular, adaptive and hardware-aware ternary-tree frameworks such as HATT[85] and Clifford-optimized heuristic mappings[84] offer structured pathways for minimizing circuit depth and two-qubit gate counts. Evaluating these emerging FTQMs across a wider set of chemically relevant systems, therefore, represents a key future direction toward achieving increasingly scalable and resource-efficient VQE and QPE implementations.

Beyond electronic-structure Hamiltonians, an important long-term extension of this framework is the incorporation of non-B.O. formulations such as NOMO, MCMO, NEO, and CNEO. Integrating these non-B.O. Hamiltonians into a unified resource-estimation workflow would enable quantitative assessments of the quantum resources required for simulations where nuclear quantum effects are non-negligible[105–116]. Developing non-B.O. Hamiltonians and ansätze for QPE and VQE, therefore, represents a promising direction for future research[117–120].

From an applied and industrial perspective, this study provides actionable insights for selecting mapping strategies, circuit optimizations, and molecular configurations compatible with specific backend constraints. From the perspective of practical VQE execution, a quantitative analysis of measurement overhead, encompassing shot-count estimation, Pauli grouping strategies, and covariance-based measurement reduction, represents an important complement to the circuit-level resource estimates presented here, and is identified as a direction for future work. The resource estimation workflow developed here can be readily extended for resource-aware benchmarking, algorithm-hardware co-design, and automated pipeline integration in quantum computational chemistry applications.

Acknowledgements

The authors would like to express their appreciation to the advisors at Qclairvoyance Quantum Labs for their support, constructive discussions, and inspiration throughout the preparation of this work.

Funding

No funding was received for this research.

Conflict of Interest

R.M. and R.V. are paid consultants at Qclairvoyance Quantum Labs. The other authors declare no competing interests.

Data Availability

The data that support the findings of this study are available in the supplementary material of this article.

References

1. Dirac, P. A. M. *The Principles of Quantum Mechanics*, chap. 1, 1–18 (Oxford University Press, Oxford, 1958), 4th edn.
2. Feynman, R. P. Simulating physics with computers. *Int. J. Theor. Phys.* **21**, 467–488, DOI: 10.1007/BF02650179 (1982).
3. Tonomura, A., Endo, J., Matsuda, T., Kawasaki, T. & Ezawa, H. Demonstration of single-electron buildup of an interference pattern. *Am. J. Phys.* **57**, 117–120, DOI: 10.1119/1.16104 (1989).
4. Zeilinger, A. Experiment and the foundations of quantum physics. *Rev. Mod. Phys.* **71**, S288–S297, DOI: 10.1103/RevModPhys.71.S288 (1999).
5. Einstein, A., Podolsky, B. & Rosen, N. Can quantum-mechanical description of physical reality be considered complete? *Phys. Rev.* **47**, 777–780, DOI: 10.1103/PhysRev.47.777 (1935).
6. Horodecki, R., Horodecki, P., Horodecki, M. & Horodecki, K. Quantum entanglement. *Rev. Mod. Phys.* **81**, 865–942, DOI: 10.1103/RevModPhys.81.865 (2009).
7. Shor, P. Algorithms for quantum computation: discrete logarithms and factoring. In *Proceedings 35th Annual Symposium on Foundations of Computer Science*, 124–134, DOI: 10.1109/SFCS.1994.365700 (1994).
8. Grover, L. K. A fast quantum mechanical algorithm for database search. In *Proceedings of the Twenty-Eighth Annual ACM Symposium on Theory of Computing*, STOC '96, 212–219, DOI: 10.1145/237814.237866 (Association for Computing Machinery, New York, NY, USA, 1996).
9. Shor, P. W. Polynomial-time algorithms for prime factorization and discrete logarithms on a quantum computer. *SIAM J. on Comput.* **26**, 1484–1509, DOI: 10.1137/S0097539795293172 (1997).
10. Nielsen, M. & Chuang, I. *Quantum Computation and Quantum Information*. Cambridge Series on Information and the Natural Sciences (Cambridge University Press, 2000).
11. Lloyd, S. Universal quantum simulators. *Science* **273**, 1073–1078, DOI: 10.1126/science.273.5278.1073 (1996).
12. Aspuru-Guzik, A., Dutoi, A. D., Love, P. J. & Head-Gordon, M. Simulated quantum computation of molecular energies. *Science* **309**, 1704–1707, DOI: 10.1126/science.1113479 (2005).
13. Harrow, A. W., Hassidim, A. & Lloyd, S. Quantum algorithm for linear systems of equations. *Phys. Rev. Lett.* **103**, 150502, DOI: 10.1103/PhysRevLett.103.150502 (2009).
14. Farhi, E., Goldstone, J. & Gutmann, S. A quantum approximate optimization algorithm (2014). 1411.4028.
15. Boyer, M., Brassard, G., Høyer, P. & Tapp, A. Tight bounds on quantum searching. *Fortschritte der Physik* **46**, 493–505, DOI: 10.1002/(SICI)1521-3978(199806)46:4/5<493::AID-PROP493>3.0.CO;2-P (1998).
16. Cao, Y. *et al.* Quantum chemistry in the age of quantum computing. *Chem. Rev.* **119**, 10856–10915, DOI: 10.1021/acs.chemrev.8b00803 (2019).
17. McArdle, S., Endo, S., Aspuru-Guzik, A., Benjamin, S. C. & Yuan, X. Quantum computational chemistry. *Rev. Mod. Phys.* **92**, 015003, DOI: 10.1103/RevModPhys.92.015003 (2020).
18. Patra, A. K. *et al.* Survey of quantum algorithms: Foundations, frameworks and applications. *Authorea* DOI: 10.22541/au.176341037.72812424/v1 (2025).
19. Bauer, B., Bravyi, S., Motta, M. & Chan, G. K.-L. Quantum algorithms for quantum chemistry and quantum materials science. *Chem. Rev.* **120**, 12685–12717, DOI: 10.1021/acs.chemrev.9b00829 (2020).
20. O'Malley, P. J. J. *et al.* Scalable quantum simulation of molecular energies. *Phys. Rev. X* **6**, 031007, DOI: 10.1103/PhysRevX.6.031007 (2016).
21. Preskill, J. Quantum Computing in the NISQ era and beyond. *Quantum* **2**, 79, DOI: 10.22331/q-2018-08-06-79 (2018).
22. Eisert, J. & Preskill, J. Mind the gaps: The fraught road to quantum advantage (2025). 2510.19928.

23. Peruzzo, A. *et al.* A variational eigenvalue solver on a photonic quantum processor. *Nat. Commun.* **5**, 4213, DOI: 10.1038/ncomms5213 (2014).

24. McClean, J. R., Romero, J., Babbush, R. & Aspuru-Guzik, A. The theory of variational hybrid quantum-classical algorithms. *New J. Phys.* **18**, 023023, DOI: 10.1088/1367-2630/18/2/023023 (2016).

25. Barkoutsos, P. K. *et al.* Quantum algorithms for electronic structure calculations: Particle-hole hamiltonian and optimized wave-function expansions. *Phys. Rev. A* **98**, 022322, DOI: 10.1103/PhysRevA.98.022322 (2018).

26. Tilly, J. *et al.* The variational quantum eigensolver: A review of methods and best practices. *Phys. Reports* **986**, 1–128, DOI: 10.1016/j.physrep.2022.08.003 (2022). The Variational Quantum Eigensolver: a review of methods and best practices.

27. Tranter, A., Love, P. J., Mintert, F. & Coveney, P. V. A comparison of the bravyi–kitaev and jordan–wigner transformations for the quantum simulation of quantum chemistry. *J. Chem. Theory Comput.* **14**, 5617–5630, DOI: 10.1021/acs.jctc.8b00450 (2018).

28. Kühn, M., Zanker, S., Deglmann, P., Marthaler, M. & Weiß, H. Accuracy and resource estimations for quantum chemistry on a near-term quantum computer. *J. Chem. Theory Comput.* **15**, 4764–4780, DOI: 10.1021/acs.jctc.9b00236 (2019).

29. Cai, Z. Resource estimation for quantum variational simulations of the hubbard model. *Phys. Rev. Appl.* **14**, 014059, DOI: 10.1103/PhysRevApplied.14.014059 (2020).

30. Johnson, P. D. *et al.* Reducing the cost of energy estimation in the variational quantum eigensolver algorithm with robust amplitude estimation (2022). 2203.07275.

31. Otten, M. *et al.* Qrechem: quantum resource estimation software for chemistry applications. *Front. Quantum Sci. Technol.* **2**, DOI: 10.3389/frqst.2023.1232624 (2023).

32. Wecker, D., Hastings, M. B. & Troyer, M. Progress towards practical quantum variational algorithms. *Phys. Rev. A* **92**, 042303, DOI: 10.1103/PhysRevA.92.042303 (2015).

33. Gonthier, J. F. *et al.* Measurements as a roadblock to near-term practical quantum advantage in chemistry: Resource analysis. *Phys. Rev. Res.* **4**, 033154, DOI: 10.1103/PhysRevResearch.4.033154 (2022).

34. Patel, S., Jayakumar, P., Yen, T.-C. & Izmaylov, A. F. Quantum measurement for quantum chemistry on a quantum computer. *Chem. Rev.* **125**, 7490–7524, DOI: 10.1021/acs.chemrev.5c00055 (2025).

35. Belaloui, N. E. *et al.* Ground-state energy estimation on current quantum hardware through the variational quantum eigensolver: A practical study. *J. Chem. Theory Comput.* **21**, 6777–6792, DOI: 10.1021/acs.jctc.4c01657 (2025).

36. Gundlach, H. *et al.* Quantum advantage in computational chemistry? (2025). 2508.20972.

37. Alexeev, Y. *et al.* A perspective on quantum computing applications in quantum chemistry using 25–100 logical qubits. *J. Chem. Theory Comput.* DOI: 10.1021/acs.jctc.5c01038 (2025).

38. Kandala, A. *et al.* Hardware-efficient variational quantum eigensolver for small molecules and quantum magnets. *Nature* **549**, 242–246, DOI: 10.1038/nature23879 (2017).

39. Leone, L., Oliviero, S. F., Cincio, L. & Cerezo, M. On the practical usefulness of the Hardware Efficient Ansatz. *Quantum* **8**, 1395, DOI: 10.22331/q-2024-07-03-1395 (2024).

40. Grimsley, H. R., Economou, S. E., Barnes, E. & Mayhall, N. J. An adaptive variational algorithm for exact molecular simulations on a quantum computer. *Nat. Commun.* **10**, 3007, DOI: 10.1038/s41467-019-10988-2 (2019).

41. Vaquero-Sabater, N., Carreras, A. & Casanova, D. Pruned-adapt-vqe: Compacting molecular ansätze by removing irrelevant operators. *J. Chem. Theory Comput.* **21**, 8720–8728, DOI: 10.1021/acs.jctc.5c00535 (2025).

42. Mondal, D., Halder, D., Halder, S. & Maitra, R. Development of a compact ansatz via operator commutativity screening: Digital quantum simulation of molecular systems. *The J. Chem. Phys.* **159**, 014105, DOI: 10.1063/5.0153182 (2023).

43. Mondal, D., Mukherjee, D. & Maitra, R. Operator commutativity screening and progressive operator block reordering toward many-body inspired quantum state preparation. *The J. Chem. Phys.* **164**, 074113, DOI: 10.1063/5.0307670 (2026).

44. Halder, D., Mondal, D. & Maitra, R. Efficient quantum state preparation through seniority driven operator selection. *The J. Chem. Phys.* **163**, 154102, DOI: 10.1063/5.0281112 (2025).

45. Halder, D., Mondal, D. & Maitra, R. Noise-independent route toward the genesis of a compact ansatz for molecular energetics: A dynamic approach. *The J. Chem. Phys.* **160**, 124104, DOI: 10.1063/5.0198277 (2024).

46. Halder, S., Dey, A., Shrikhande, C. & Maitra, R. Machine learning assisted construction of a shallow depth dynamic ansatz for noisy quantum hardware. *Chem. Sci.* **15**, 3279–3289, DOI: 10.1039/D3SC05807G (2024).

47. Halder, S., Anand, K. & Maitra, R. Construction of chemistry-inspired dynamic ansatz utilizing generative machine learning. *The J. Phys. Chem. A* **129**, 5889–5900, DOI: 10.1021/acs.jpca.5c02346 (2025).

48. Romero, J. *et al.* Strategies for quantum computing molecular energies using the unitary coupled cluster ansatz. *Quantum Sci. Technol.* **4**, 014008, DOI: 10.1088/2058-9565/aad3e4 (2018).

49. Bravyi, S., Gambetta, J. M., Mezzacapo, A. & Temme, K. Tapering off qubits to simulate fermionic hamiltonians (2017). 1701.08213.

50. Jordan, P. & Wigner, E. Über das paulische äquivalenzverbot. *Zeitschrift für Physik* **47**, 631–651, DOI: 10.1007/BF01331938 (1928).

51. Nielsen, M. A. *et al.* The fermionic canonical commutation relations and the jordan-wigner transform. *Sch. Phys. Sci. The Univ. Qld.* **59**, 75 (2005).

52. Bravyi, S. B. & Kitaev, A. Y. Fermionic quantum computation. *Annals Phys.* **298**, 210–226, DOI: 10.1006/aphy.2002.6254 (2002).

53. Seeley, J. T., Richard, M. J. & Love, P. J. The bravyi-kitaev transformation for quantum computation of electronic structure. *The J. Chem. Phys.* **137**, 224109, DOI: 10.1063/1.4768229 (2012).

54. Tranter, A. *et al.* The bravyi–kitaev transformation: Properties and applications. *Int. J. Quantum Chem.* **115**, 1431–1441, DOI: 10.1002/qua.24969 (2015).

55. Szabo, A. & Ostlund, N. S. *Modern Quantum Chemistry: Introduction to Advanced Electronic Structure Theory*, chap. 2, 39–107. Dover Books on Chemistry (Dover Publications, Mineola, NY, 1996), 1st, revised edn.

56. Helgaker, T., Jørgensen, P. & Olsen, J. *Molecular Electronic-Structure Theory*, chap. 1, 1–33 (John Wiley & Sons, Ltd, 2000), 1st edn.

57. Born, M. & Huang, K. *Dynamical Theory of Crystal Lattices* (Clarendon Press, Oxford, 1954).

58. Fetter, A. L. & Walecka, J. D. *Quantum Theory of Many-Particle Systems*, chap. 1, 3–32. Dover Books on Physics (Dover Publications, Mineola, New York, 2003). Corrected reprint of the 7th printing (McGraw-Hill, 1971).

59. Shavitt, I. & Bartlett, R. J. *Many-Body Methods in Chemistry and Physics: MBPT and Coupled-Cluster Theory*, chap. 2, 54–90. Cambridge Molecular Science (Cambridge University Press, Cambridge, 2009), 1st edn. Chapter 2.

60. Born, M. & Oppenheimer, R. Zur quantentheorie der molekeln. *Annalen der Physik* **389**, 457–484, DOI: 10.1002/andp.19273892002 (1927).

61. Thomas, I. L. Protonic structure of molecules. i. ammonia molecules. *Phys. Rev.* **185**, 90–94, DOI: 10.1103/PhysRev.185.90 (1969).

62. Thomas, I. The protonic structure of methane, ammonia, water, and hydrogen fluoride. *Chem. Phys. Lett.* **3**, 705–706, DOI: 10.1016/0009-2614(69)87015-6 (1969).

63. Tachikawa, M., Mori, K., Nakai, H. & Iguchi, K. An extension of ab initio molecular orbital theory to nuclear motion. *Chem. Phys. Lett.* **290**, 437–442, DOI: 10.1016/S0009-2614(98)00519-3 (1998).

64. Nakai, H., Sodeyama, K. & Hoshino, M. Non-born–oppenheimer theory for simultaneous determination of vibrational and electronic excited states: ab initio no+mo/cis theory. *Chem. Phys. Lett.* **345**, 118–124, DOI: 10.1016/S0009-2614(01)00836-3 (2001).

65. Nakai, H. Simultaneous determination of nuclear and electronic wave functions without born–oppenheimer approximation: Ab initio no+mo/hf theory. *Int. J. Quantum Chem.* **86**, 511–517, DOI: 10.1002/qua.1106 (2002).

66. Nakai, H. & Sodeyama, K. Many-body effects in nonadiabatic molecular theory for simultaneous determination of nuclear and electronic wave functions: Ab initio nomo/mbpt and cc methods. *The J. Chem. Phys.* **118**, 1119–1127, DOI: 10.1063/1.1528951 (2003).

67. Nakai, H. Nuclear orbital plus molecular orbital theory: Simultaneous determination of nuclear and electronic wave functions without born–oppenheimer approximation. *Int. J. Quantum Chem.* **107**, 2849–2869, DOI: 10.1002/qua.21379 (2007).

68. Tachikawa, M. Simultaneous optimization of gaussian type function exponents for electron and positron with full-ci wavefunction – application to ground and excited states of positronic compounds with multi-component molecular orbital approach. *Chem. Phys. Lett.* **350**, 269–276, DOI: 10.1016/S0009-2614(01)01286-6 (2001).

69. Ishimoto, T., Tachikawa, M. & Nagashima, U. Review of multicomponent molecular orbital method for direct treatment of nuclear quantum effect. *Int. J. Quantum Chem.* **109**, 2677–2694, DOI: 10.1002/qua.22069 (2009).

70. Webb, S. P., Iordanov, T. & Hammes-Schiffer, S. Multiconfigurational nuclear-electronic orbital approach: Incorporation of nuclear quantum effects in electronic structure calculations. *The J. Chem. Phys.* **117**, 4106–4118, DOI: 10.1063/1.1494980 (2002).

71. Pavošević, F., Culpitt, T. & Hammes-Schiffer, S. Multicomponent quantum chemistry: Integrating electronic and nuclear quantum effects via the nuclear–electronic orbital method. *Chem. Rev.* **120**, 4222–4253, DOI: 10.1021/acs.chemrev.9b00798 (2020).

72. Xu, X. & Yang, Y. Constrained nuclear-electronic orbital density functional theory: Energy surfaces with nuclear quantum effects. *The J. Chem. Phys.* **152**, 084107, DOI: 10.1063/1.5143371 (2020).

73. Xu, X. & Yang, Y. Full-quantum descriptions of molecular systems from constrained nuclear–electronic orbital density functional theory. *The J. Chem. Phys.* **153**, 074106, DOI: 10.1063/5.0014001 (2020).

74. Culpitt, T., Chen, Z., Pavošević, F. & Yang, Y. Constrained nuclear-electronic orbital theory for quantum computation. *J. Chem. Theory Comput.* **21**, 7845–7854, DOI: 10.1021/acs.jctc.5c00815 (2025).

75. Hehre, W. J., Stewart, R. F. & Pople, J. A. Self-consistent molecular-orbital methods. i. use of gaussian expansions of slater-type atomic orbitals. *The J. Chem. Phys.* **51**, 2657–2664, DOI: 10.1063/1.1672392 (1969).

76. Dunning, J., Thom H. Gaussian basis sets for use in correlated molecular calculations. i. the atoms boron through neon and hydrogen. *The J. Chem. Phys.* **90**, 1007–1023, DOI: 10.1063/1.456153 (1989).

77. Fock, V. Konfigurationsraum und zweite quantelung. *Zeitschrift für Physik* **75**, 622–647, DOI: 10.1007/BF01344458 (1932).

78. Steudtner, M. & Wehner, S. Fermion-to-qubit mappings with varying resource requirements for quantum simulation. *New J. Phys.* **20**, 063010, DOI: 10.1088/1367-2630/aac54f (2018).

79. Jiang, Z., Kalev, A., Mruczkiewicz, W. & Neven, H. Optimal fermion-to-qubit mapping via ternary trees with applications to reduced quantum states learning. *Quantum* **4**, 276, DOI: 10.22331/q-2020-06-04-276 (2020).

80. Derby, C., Klassen, J., Bausch, J. & Cubitt, T. Compact fermion to qubit mappings. *Phys. Rev. B* **104**, 035118, DOI: 10.1103/PhysRevB.104.035118 (2021).

81. Miller, A., Zimborás, Z., Knecht, S., Maniscalco, S. & García-Pérez, G. Bonsai algorithm: Grow your own fermion-to-qubit mappings. *PRX Quantum* **4**, 030314, DOI: 10.1103/PRXQuantum.4.030314 (2023).

82. O'Brien, O. & Strelchuk, S. Ultrafast hybrid fermion-to-qubit mapping. *Phys. Rev. B* **109**, 115149, DOI: 10.1103/PhysRevB.109.115149 (2024).

83. Parella-Dilmé, T. *et al.* Reducing entanglement with physically inspired fermion-to-qubit mappings. *PRX Quantum* **5**, 030333, DOI: 10.1103/PRXQuantum.5.030333 (2024).

84. Yu, J., Liu, Y., Sugiura, S., Van Voorhis, T. & Zeytinoğlu, S. Clifford circuit-based heuristic optimization of fermion-to-qubit mappings. *J. Chem. Theory Comput.* **21**, 9430–9443, DOI: 10.1021/acs.jctc.5c00794 (2025).

85. Liu, Y. *et al.* Hatt: Hamiltonian adaptive ternary tree for optimizing fermion-to-qubit mapping. In *2025 IEEE International Symposium on High Performance Computer Architecture (HPCA)*, 143–157, DOI: 10.1109/HPCA61900.2025.00022 (2025).

86. Roos, B. O., Taylor, P. R. & Sigbahn, P. E. A complete active space scf method (casscf) using a density matrix formulated super-ci approach. *Chem. Phys.* **48**, 157–173, DOI: 10.1016/0301-0104(80)80045-0 (1980).

87. Battaglia, S., Rossmannek, M., Rybkin, V. V., Tavernelli, I. & Hutter, J. A general framework for active space embedding methods with applications in quantum computing. *npj Comput. Mater.* **10**, 297, DOI: 10.1038/s41524-024-01477-2 (2024).

88. Gard, B. T. *et al.* Efficient symmetry-preserving state preparation circuits for the variational quantum eigensolver algorithm. *npj Quantum Inf.* **6**, 10, DOI: 10.1038/s41534-019-0240-1 (2020).

89. Setia, K. *et al.* Reducing qubit requirements for quantum simulations using molecular point group symmetries. *J. Chem. Theory Comput.* **16**, 6091–6097, DOI: 10.1021/acs.jctc.0c00113 (2020).

90. Seki, K., Shirakawa, T. & Yunoki, S. Symmetry-adapted variational quantum eigensolver. *Phys. Rev. A* **101**, 052340, DOI: 10.1103/PhysRevA.101.052340 (2020).

91. Fock, V. Näherungsmethode zur lösung des quantenmechanischen mehrkörperproblems. *Zeitschrift für Physik* **61**, 126–148, DOI: 10.1007/BF01340294 (1930).

92. Van Rossum, G. Python tutorial. Tech. Rep. CS-R9526, Centrum voor Wiskunde en Informatica (CWI) (1995).

93. Python Software Foundation. *Python Language Reference, v3.11* (2022). Accessed: 2025-11-18.

94. Harris, C. R. *et al.* Array programming with NumPy. *Nature* **585**, 357–362, DOI: 10.1038/s41586-020-2649-2 (2020).

95. Sun, Q. Libcint: An efficient general integral library for gaussian basis functions. *J. Comput. Chem.* **36**, 1664–1671, DOI: https://doi.org/10.1002/jcc.23981 (2015).

96. Sun, Q. *et al.* Pyscf: the python-based simulations of chemistry framework. *WIREs Comput. Mol. Sci.* **8**, e1340, DOI: https://doi.org/10.1002/wcms.1340 (2018).

97. Sun, Q. *et al.* Recent developments in the pyscf program package. *The J. Chem. Phys.* **153**, 024109, DOI: 10.1063/5.0006074 (2020).

98. Javadi-Abhari, A. *et al.* Quantum computing with qiskit (2024). 2405.08810.

99. Qiskit Community. Qiskit aer v0.15.1. https://pypi.org/project/qiskit-aer/0.15.1/ (2024). Accessed: 2025-11-18.

100. The Qiskit Nature Developers and Contributors. Qiskit nature, DOI: 10.5281/zenodo.7828768 (2023).

101. Hanwell, M. D. *et al.* Avogadro: an advanced semantic chemical editor, visualization, and analysis platform. *J. Cheminformatics* **4**, 17, DOI: 10.1186/1758-2946-4-17 (2012).

102. Rappe, A. K., Casewit, C. J., Colwell, K. S., Goddard, W. A. I. & Skiff, W. M. Uff, a full periodic table force field for molecular mechanics and molecular dynamics simulations. *J. Am. Chem. Soc.* **114**, 10024–10035, DOI: 10.1021/ja00051a040 (1992).

103. IBM Quantum & Qiskit Development Team. Qiskit API Reference: UnitaryGate (Version 1.3). https://quantum.cloud.ibm.com/docs/en/api/qiskit/1.3/qiskit.circuit.library.UnitaryGate (2024). Accessed: 2026-02-19.

104. Qiskit Development Team. *Qiskit SDK Docs: Qiskit Circuit Library - v1.3.3*. IBM Quantum (2025). Accessed: 2025-11-07.

105. Hammes-Schiffer, S. & Tully, J. C. Proton transfer in solution: Molecular dynamics with quantum transitions. *The J. Chem. Phys.* **101**, 4657–4667, DOI: 10.1063/1.467455 (1994).

106. Tuckerman, M. E., Marx, D., Klein, M. L. & Parrinello, M. On the quantum nature of the shared proton in hydrogen bonds. *Science* **275**, 817–820, DOI: 10.1126/science.275.5301.817 (1997).

107. Morrone, J. A. & Car, R. Nuclear quantum effects in water. *Phys. Rev. Lett.* **101**, 017801, DOI: 10.1103/PhysRevLett.101.017801 (2008).

108. Reece, S. Y. & Nocera, D. G. Proton-coupled electron transfer in biology: Results from synergistic studies in natural and model systems. *Annu. Rev. Biochem.* **78**, 673–699, DOI: https://doi.org/10.1146/annurev.biochem.78.080207.092132 (2009).

109. Li, X.-Z., Walker, B. & Michaelides, A. Quantum nature of the hydrogen bond. *Proc. Natl. Acad. Sci.* **108**, 6369–6373, DOI: 10.1073/pnas.1016653108 (2011).

110. Klinman, J. P. & Kohen, A. Hydrogen tunneling links protein dynamics to enzyme catalysis. *Annu. Rev. Biochem.* **82**, 471–496, DOI: https://doi.org/10.1146/annurev-biochem-051710-133623 (2013).

111. Wang, L., Fried, S. D., Boxer, S. G. & Markland, T. E. Quantum delocalization of protons in the hydrogen-bond network of an enzyme active site. *Proc. Natl. Acad. Sci.* **111**, 18454–18459, DOI: 10.1073/pnas.1417923111 (2014).

112. Ceriotti, M. *et al.* Nuclear quantum effects in water and aqueous systems: Experiment, theory, and current challenges. *Chem. Rev.* **116**, 7529–7550, DOI: 10.1021/acs.chemrev.5b00674 (2016).

113. Markland, T. E. & Ceriotti, M. Nuclear quantum effects enter the mainstream. *Nat. Rev. Chem.* **2**, 0109, DOI: 10.1038/s41570-017-0109 (2018).

114. Li, M., Wang, P., Yu, X., Su, Y. & Zhao, J. Impact of nuclear quantum effects on the structural properties of protonated water clusters. *The J. Phys. Chem. A* **128**, 5954–5962, DOI: 10.1021/acs.jpca.4c03340 (2024).

115. Han, E., Fang, W. & Chen, J. Nuclear quantum effects in two-hydrogen intermediates on graphene-embedded transition metal atoms. *Phys. Chem. Chem. Phys.* **27**, 12542–12549, DOI: 10.1039/D5CP00820D (2025).

116. Ugur, B. E. & Webb, M. A. Nuclear quantum effects in molecular liquids across chemical space. *Nat. Commun.* **16**, 5786, DOI: 10.1038/s41467-025-60850-x (2025).

117. Veis, L., Višňák, J., Nishizawa, H., Nakai, H. & Pittner, J. Quantum chemistry beyond born–oppenheimer approximation on a quantum computer: A simulated phase estimation study. *Int. J. Quantum Chem.* **116**, 1328–1336, DOI: https://doi.org/10.1002/qua.25176 (2016).

118. Kovyrshin, A. *et al.* A quantum computing implementation of nuclearelectronic orbital (neo) theory: Toward an exact pre-born–oppenheimer formulation of molecular quantum systems. *The J. Chem. Phys.* **158**, 214119, DOI: 10.1063/5.0150291 (2023).

119. Nykänen, A. *et al.* Toward accurate post-born–oppenheimer molecular simulations on quantum computers: An adaptive variational eigensolver with nuclear-electronic frozen natural orbitals. *J. Chem. Theory Comput.* **19**, 9269–9277, DOI: 10.1021/acs.jctc.3c01091 (2023).

120. Cabral, D. G. A. *et al.* Error-mitigation enabled multicomponent quantum simulations beyond the born-oppenheimer approximation (2025). 2511.11941.

Supplementary Information

This Supplementary Information provides detailed structural and raw resource data supporting the analysis presented in Section 4 of the main manuscript. The contents are organised to ensure full transparency and reproducibility of the quantum resource estimation workflow.

First, we report the molecular geometries used throughout the study. For the small illustrative systems (CH_4 and CH_3F), force-field-optimised coordinates generated using the `Avogadro` molecular editor with the universal force field (UFF) are provided in Table S1. For all 13 benchmark molecules used in the scalability analysis, coupled-cluster singles and doubles (CCSD) optimised geometries at the STO-3G level of theory, computed using `PySCF`, are listed in Table S2. All coordinates are reported in Å and rounded to four decimal places. Atom ordering follows the corresponding `.xyz` file outputs to ensure direct reproducibility.

Second, we provide complete raw Hamiltonian- and circuit-level resource counts for every molecule, fermion-to-qubit mapping (Jordan–Wigner, Bravyi–Kitaev, and Parity), and reduction configuration (no tapering/no frozen core, tapering only, frozen core only, and both combined) in Tables S3 and S4. Reported quantities include spin-orbital counts, Hamiltonian term counts, Pauli string statistics, individual Pauli operator counts, circuit width, circuit depth, total gate counts, and number of variational parameters.

Finally, we include explicit reduction factors computed relative to the no-tapering/no-frozen-core baseline for each molecule and mapping in Table S5. These tables provide the numerical basis for all percentage and multiplicative reductions discussed in the main text.

Together, these data ensure that all reported scaling trends, resource reductions, and comparative statements in the manuscript are fully traceable to their underlying raw quantities.

Table S1. Force-field-optimised atomic coordinates (Å) for CH_4 and CH_3F, as generated by the `Avogadro` molecular editor[101] using the built-in universal force field (UFF) auto-optimisation tool[102]. These geometries serve as illustrative inputs for the resource-estimation workflow presented in Section 4 and are not intended as high-accuracy reference structures. Atom ordering follows the output of the `.xyz` file produced by Avogadro.

Molecule	Atom	x (Å)	y (Å)	z (Å)
Methane (CH_4)	C	−4.9566	4.6276	0.00000
	H	−5.8816	4.7456	−0.5688
	H	−4.9356	5.3539	0.8155
	H	−4.9085	3.6170	0.4113
	H	−4.1009	4.7941	−0.6580
Fluoromethane (CH_3F)	C	−4.9578	4.5872	−0.0454
	H	−5.8862	4.7153	−0.6056
	F	−4.9316	5.4894	0.9676
	H	−4.9092	3.5822	0.3785
	H	−4.0983	4.7641	−0.6951

Table S2. CCSD-optimised atomic coordinates (Å) for all 13 molecules used in the scalability analysis of Section 4. Geometry optimisations were performed at the CCSD/STO-3G level of theory using the `PySCF` quantum chemistry package[97], with the `geometric` solver employed for the optimisation procedure. Coordinates are reported to four decimal places. Atom ordering follows the output of the `.xyz` files produced by`PySCF`.

Molecule	Atom	x (Å)	y (Å)	z (Å)
Hydrogen (H_2)	H	−8.0162	4.7102	0.0247
	H	−8.6385	4.7896	−0.3580
Lithium Hydride (LiH)	Li	−1.3219	3.0763	0.0338
	H	−0.6203	2.1491	1.0550
Hydrogen Fluoride (HF)	F	−9.3450	1.4356	0.0011
	H	−8.3880	1.6991	−0.0613

Continued on next page

Table S2. (*continued*)

Molecule	Atom	x (Å)	y (Å)	z (Å)
Beryllium Hydride (BeH_2)	Be	−0.9837	3.4084	0.1009
	H	−1.6817	2.9596	−0.9204
	H	−0.2858	3.8573	1.1222
Water (H_2O)	O	−8.6489	5.1126	−0.0409
	H	−7.6855	5.4719	−0.0364
	H	−9.0487	5.8301	0.5778
Ammonia (NH_3)	N	−9.0469	4.1587	0.0508
	H	−8.5555	3.4144	0.6423
	H	−8.3995	4.1782	−0.8012
	H	−9.8569	3.5804	−0.3427
Methane (CH_4)	C	−8.4804	4.2914	0.0000
	H	−9.3089	3.5933	−0.2316
	H	−8.3381	4.3446	1.0974
	H	−7.5481	3.9287	−0.4761
	H	−8.7263	5.2988	−0.3898
Dioxygen (O_2)	O	−4.9031	4.1890	0.0000
	O	−3.5919	4.1890	0.0000
Dinitrogen (N_2)	N	−6.3552	5.1689	0.0000
	N	−5.1664	5.1830	0.0000
Carbon Monoxide (CO)	C	−2.7667	3.5605	0.0000
	O	−1.6051	3.3407	0.0000
Acetylene (C_2H_2)	C	−6.9042	3.9642	0.0000
	C	−5.6920	3.9898	0.0000
	H	−7.9918	3.9412	0.0000
	H	−4.6045	4.0127	0.0001
Hydrogen Peroxide (H_2O_2)	O	−2.5277	−0.0366	0.0629
	O	−1.0578	−0.0276	−0.0629
	H	−2.7408	0.1269	−0.9414
	H	−0.8446	−0.1911	0.9414
Ethylene (C_2H_4)	C	−7.0983	3.3615	0.0000
	C	−5.7441	3.3984	0.0000
	H	−7.7080	4.2843	0.0000
	H	−7.6569	2.4070	0.0000
	H	−5.1855	4.3529	0.0000
	H	−5.1344	2.4756	0.0000

Table S3. Raw circuit resource counts for all molecules, mappers, and tapering/frozen-core combinations. Columns show: number of spin orbitals (N_{so}), Hamiltonian terms (N_{sqh}), Pauli strings (N_{PS}), total Pauli operators (N_{PO}), and individual Pauli operator counts (N_X, N_Y, N_Z, N_I). Mapper abbreviations: JW = Jordan–Wigner, BK = Bravyi–Kitaev, P = Parity. Combo: (-) = no tapering/no frozen core (baseline), (T) = tapering only, (F) = frozen core only, (TF) = both.

Molecule	Mapper	Tap.	FC	Combo	N_{so}	N_{sqh}	N_{PS}	N_{PO}	N_X	N_Y	N_Z	N_I
H_2	JW	**False**	**False**	**-**	**4**	**36**	**15**	**60**	**8**	**8**	**16**	**28**
		True	False	T	4	36	3	3	1	0	1	1
		False	True	F	4	36	15	60	8	8	16	28
		True	True	TF	4	36	3	3	1	0	1	1
	BK	**False**	**False**	**-**	**4**	**36**	**15**	**60**	**8**	**0**	**26**	**26**
		True	False	T	4	36	3	3	1	0	1	1
		False	True	F	4	36	15	60	8	0	26	26
		True	True	TF	4	36	3	3	1	0	1	1
	P	**False**	**False**	**-**	**4**	**36**	**5**	**10**	**2**	**0**	**4**	**4**
		True	False	T	4	36	3	3	1	0	1	1
		False	True	F	4	36	5	10	2	0	4	4
		True	True	TF	4	36	3	3	1	0	1	1
LiH	JW	**False**	**False**	**-**	**12**	**1,860**	**631**	**7,572**	**840**	**840**	**1,568**	**4,324**
		True	False	T	12	1,860	558	4,464	690	426	1,244	2,104
		False	True	F	10	810	276	2,760	332	332	576	1,520
		True	True	TF	10	810	231	1,386	246	134	396	610
	BK	**False**	**False**	**-**	**12**	**1,860**	**631**	**7,572**	**1,244**	**976**	**1,440**	**3,912**
		True	False	T	12	1,860	558	4,464	756	594	1,127	1,987
		False	True	F	10	810	276	2,760	442	402	566	1,350
		True	True	TF	10	810	231	1,386	244	216	425	501
	P	**False**	**False**	**-**	**12**	**1,860**	**631**	**6,310**	**1,480**	**624**	**1,004**	**3,202**
		True	False	T	12	1,860	558	4,464	1,036	510	978	1,940
		False	True	F	10	810	276	2,208	512	240	420	1,036
		True	True	TF	10	810	231	1,386	316	178	366	526
HF	JW	**False**	**False**	**-**	**12**	**1,860**	**631**	**7,572**	**840**	**840**	**1,568**	**4,324**
		True	False	T	12	1,860	558	4,464	690	426	1,244	2,104
		False	True	F	10	810	276	2,760	332	332	576	1,520
		True	True	TF	10	810	231	1,386	246	134	396	610
	BK	**False**	**False**	**-**	**12**	**1,860**	**631**	**7,572**	**1,244**	**976**	**1,440**	**3,912**
		True	False	T	12	1,860	558	4,464	756	594	1,127	1,987
		False	True	F	10	810	276	2,760	442	402	566	1,350
		True	True	TF	10	810	231	1,386	244	216	425	501

Continued on next page

Table S3. (*continued*)

Molecule	Mapper	Tap.	FC	Combo	N_{so}	N_{sqh}	N_{PS}	N_{PO}	N_X	N_Y	N_Z	N_I
	P	**False**	**False**	**-**	**12**	**1,860**	**631**	**6,310**	**1,480**	**624**	**1,004**	**3,202**
		True	False	T	12	1,860	558	4,464	1,036	510	978	1,940
		False	True	F	10	810	276	2,208	512	240	420	1,036
		True	True	TF	10	810	231	1,386	316	178	366	526
BeH_2	JW	**False**	**False**	**-**	**14**	**2,014**	**666**	**9,324**	**912**	**912**	**2,052**	**5,448**
		True	False	T	14	2,014	596	5,364	686	482	1,706	2,490
		False	True	F	12	1,012	327	3,924	408	408	856	2,252
		True	True	TF	12	1,012	268	1,876	268	180	632	796
	BK	**False**	**False**	**-**	**14**	**2,014**	**666**	**9,324**	**1,362**	**1,174**	**1,436**	**5,352**
		True	False	T	14	2,014	596	5,364	848	724	1,512	2,280
		False	True	F	12	1,012	327	3,924	614	478	760	2,072
		True	True	TF	12	1,012	268	1,876	302	240	506	828
	P	**False**	**False**	**-**	**14**	**2,014**	**666**	**7,992**	**1,948**	**708**	**1,132**	**4,204**
		True	False	T	14	2,014	596	5,364	1,130	652	1,233	2,349
		False	True	F	12	1,012	327	3,270	768	320	540	1,642
		True	True	TF	12	1,012	268	1,876	396	266	478	736
H_2O	JW	**False**	**False**	**-**	**14**	**3,170**	**1,094**	**15,316**	**1,604**	**1,604**	**3,164**	**8,944**
		True	False	T	14	3,170	1,052	11,572	1,506	1,046	2,995	6,025
		False	True	F	12	1,608	555	6,660	772	772	1,344	3,772
		True	True	TF	12	1,608	527	4,743	712	460	1,219	2,352
	BK	**False**	**False**	**-**	**14**	**3,170**	**1,094**	**15,316**	**2,282**	**1,980**	**2,341**	**8,713**
		True	False	T	14	3,170	1,052	11,572	1,900	1,520	2,217	5,935
		False	True	F	12	1,608	555	6,660	1,176	962	1,166	3,356
		True	True	TF	12	1,608	527	4,743	810	646	1,013	2,274
	P	**False**	**False**	**-**	**14**	**3,170**	**1,094**	**13,128**	**3,108**	**1,240**	**1,822**	**6,958**
		True	False	T	14	3,170	1,052	11,572	2,636	1,208	1,880	5,848
		False	True	F	12	1,608	555	5,550	1,304	572	884	2,790
		True	True	TF	12	1,608	527	4,743	1,054	554	890	2,245
NH_3	JW	**False**	**False**	**-**	**16**	**10,904**	**3,633**	**58,128**	**5,952**	**5,952**	**12,272**	**33,952**
		True	False	T	16	10,904	3,633	50,862	5,900	4,720	12,480	27,762
		False	True	F	14	7,086	2,342	32,788	3,772	3,772	6,796	18,448
		True	True	TF	14	7,086	2,342	28,104	3,740	2,876	7,016	14,472
	BK	**False**	**False**	**-**	**16**	**10,904**	**3,633**	**58,128**	**7,140**	**6,364**	**9,792**	**34,832**

Continued on next page

Table S3. (*continued*)

Molecule	Mapper	Tap.	FC	Combo	N_{so}	N_{sqh}	N_{PS}	N_{PO}	N_X	N_Y	N_Z	N_I
		True	False	T	16	10,904	3,633	50,862	7,140	6,364	8,332	29,026
		False	True	F	14	7,086	2,342	32,788	5,248	4,680	4,690	18,170
		True	True	TF	14	7,086	2,342	28,104	4,618	3,812	4,615	15,059
	P	**False**	**False**	**-**	**16**	**10,904**	**3,633**	**50,862**	**12,572**	**4,676**	**6,130**	**27,484**
		True	False	T	16	10,904	3,633	50,862	12,572	4,676	6,130	27,484
		False	True	F	14	7,086	2,342	28,104	7,072	2,812	3,854	14,366
		True	True	TF	14	7,086	2,342	28,104	7,072	2,812	3,854	14,366
CH_4	JW	**False**	**False**	**-**	**18**	**21,514**	**6,936**	**124,848**	**11,804**	**11,804**	**25,232**	**76,008**
		True	False	T	18	21,514	6,936	110,976	11,732	9,668	25,820	63,756
		False	True	F	16	14,780	4,721	75,536	7,888	7,888	14,980	44,780
		True	True	TF	16	14,780	4,721	66,094	7,852	6,204	15,724	36,314
	BK	**False**	**False**	**-**	**18**	**21,514**	**6,936**	**124,848**	**17,202**	**14,682**	**18,988**	**73,976**
		True	False	T	18	21,514	6,936	110,976	15,592	13,062	18,476	63,846
		False	True	F	16	14,780	4,721	75,536	9,736	8,864	11,392	45,544
		True	True	TF	16	14,780	4,721	66,094	9,736	8,864	9,990	37,504
	P	**False**	**False**	**-**	**18**	**21,514**	**6,936**	**110,976**	**26,120**	**9,412**	**12,428**	**63,016**
		True	False	T	18	21,514	6,936	110,976	26,120	9,412	12,428	63,016
		False	True	F	16	14,780	4,721	66,094	15,700	6,032	8,276	36,086
		True	True	TF	16	14,780	4,721	66,094	15,700	6,032	8,276	36,086
O_2	JW	**False**	**False**	**-**	**20**	**6,348**	**2,239**	**44,780**	**3,600**	**3,600**	**9,704**	**27,876**
		True	False	T	20	6,348	2,229	33,435	2,992	2,396	10,018	18,029
		False	True	F	16	2,328	825	13,200	1,256	1,256	2,748	7,940
		True	True	TF	16	2,328	815	8,965	960	732	3,004	4,269
	BK	**False**	**False**	**-**	**20**	**6,348**	**2,239**	**44,780**	**5,714**	**4,698**	**6,416**	**27,952**
		True	False	T	20	6,348	2,229	33,435	3,788	3,634	9,403	16,610
		False	True	F	16	2,328	825	13,200	1,500	1,340	2,106	8,254
		True	True	TF	16	2,328	815	8,965	1,210	1,162	2,499	4,094
	P	**False**	**False**	**-**	**20**	**6,348**	**2,239**	**40,302**	**9,580**	**3,052**	**3,940**	**23,730**
		True	False	T	20	6,348	2,229	33,435	6,586	3,928	6,948	15,973
		False	True	F	16	2,328	825	11,550	2,676	1,016	1,420	6,438
		True	True	TF	16	2,328	815	8,965	1,590	1,306	2,222	3,847
N_2	JW	**False**	**False**	**-**	**20**	**8,268**	**2,951**	**59,020**	**4,992**	**4,992**	**12,400**	**36,636**
		True	False	T	20	8,268	2,951	47,216	4,288	3,650	13,514	25,764
		False	True	F	16	3,288	1,177	18,832	1,928	1,928	3,768	11,208

Continued on next page

Table S3. (*continued*)

Molecule	Mapper	Tap.	FC	Combo	N_{so}	N_{sqh}	N_{PS}	N_{PO}	N_X	N_Y	N_Z	N_I
		True	True	TF	16	3,288	1,177	14,124	1,580	1,290	4,116	7,138
	BK	**False**	**False**	**-**	**20**	**8,268**	**2,951**	**59,020**	**8,144**	**6,456**	**8,121**	**36,299**
		True	False	T	20	8,268	2,951	47,216	5,914	5,038	13,464	22,800
		False	True	F	16	3,288	1,177	18,832	2,292	2,032	2,858	11,650
		True	True	TF	16	3,288	1,177	14,124	1,964	1,728	3,956	6,476
	P	**False**	**False**	**-**	**20**	**8,268**	**2,951**	**53,118**	**12,648**	**4,024**	**5,164**	**31,282**
		True	False	T	20	8,268	2,951	47,216	10,016	5,016	7,474	24,710
		False	True	F	16	3,288	1,177	16,478	3,888	1,456	1,996	9,138
		True	True	TF	16	3,288	1,177	14,124	3,070	1,578	2,600	6,876
CO	JW	**False**	**False**	**-**	**20**	**16,576**	**5,827**	**116,540**	**9,756**	**9,756**	**25,544**	**71,484**
		True	False	T	20	16,576	5,827	99,059	9,030	7,560	26,134	56,335
		False	True	F	16	6,648	2,329	37,264	3,752	3,752	7,744	22,016
		True	True	TF	16	6,648	2,329	30,277	3,390	2,696	8,192	15,999
	BK	**False**	**False**	**-**	**20**	**16,576**	**5,827**	**116,540**	**16,576**	**13,104**	**16,750**	**70,110**
		True	False	T	20	16,576	5,827	99,059	12,456	10,792	23,434	52,377
		False	True	F	16	6,648	2,329	37,264	4,608	4,252	5,808	22,596
		True	True	TF	16	6,648	2,329	30,277	4,412	3,688	7,384	14,793
	P	**False**	**False**	**-**	**20**	**16,576**	**5,827**	**104,886**	**25,628**	**8,304**	**10,200**	**60,754**
		True	False	T	20	16,576	5,827	99,059	22,524	9,112	13,490	53,933
		False	True	F	16	6,648	2,329	32,606	7,804	3,052	3,932	17,818
		True	True	TF	16	6,648	2,329	30,277	6,644	3,452	5,256	14,925
C_2H_2	JW	**False**	**False**	**-**	**24**	**59,084**	**13,085**	**314,040**	**21,780**	**21,780**	**68,056**	**202,424**
		True	False	T	24	59,084	13,085	287,870	21,584	18,212	71,512	176,562
		False	True	F	20	30,136	6,479	129,580	10,616	10,616	27,096	81,252
		True	True	TF	20	30,136	6,479	116,622	10,476	8,548	28,444	69,154
	BK	**False**	**False**	**-**	**24**	**59,084**	**13,085**	**314,040**	**38,704**	**28,410**	**40,889**	**206,037**
		True	False	T	24	59,084	13,085	287,870	31,188	26,370	35,325	194,987
		False	True	F	20	30,136	6,479	129,580	17,672	13,598	18,327	79,983
		True	True	TF	20	30,136	6,479	116,622	14,738	12,184	17,025	72,675
	P	**False**	**False**	**-**	**24**	**59,084**	**13,085**	**287,870**	**68,464**	**18,372**	**23,524**	**177,510**
		True	False	T	24	59,084	13,085	287,870	68,464	18,372	23,524	177,510
		False	True	F	20	30,136	6,479	116,622	27,356	8,772	11,336	69,158
		True	True	TF	20	30,136	6,479	116,622	27,356	8,772	11,336	69,158

Continued on next page

Table S3. (*continued*)

Molecule	Mapper	Tap.	FC	Combo	N_{so}	N_{sqh}	N_{PS}	N_{PO}	N_X	N_Y	N_Z	N_I
H_2O_2	JW	**False**	**False**	**-**	**24**	**39,404**	**10,885**	**261,240**	**18,580**	**18,580**	**56,104**	**167,976**
		True	False	T	24	39,404	10,885	239,470	18,384	15,848	58,940	146,298
		False	True	F	20	19,804	5,639	112,780	9,496	9,496	23,636	70,152
		True	True	TF	20	19,804	5,639	101,502	9,368	7,708	24,844	59,582
	BK	**False**	**False**	**-**	**24**	**39,404**	**10,885**	**261,240**	**32,532**	**24,510**	**33,677**	**170,521**
		True	False	T	24	39,404	10,885	239,470	26,168	22,894	29,289	161,119
		False	True	F	20	19,804	5,639	112,780	15,640	12,294	15,917	68,929
		True	True	TF	20	19,804	5,639	101,502	13,050	11,032	14,831	62,589
	P	**False**	**False**	**-**	**24**	**39,404**	**10,885**	**239,470**	**56,700**	**15,752**	**19,492**	**147,526**
		True	False	T	24	39,404	10,885	239,470	56,700	15,752	19,492	147,526
		False	True	F	20	19,804	5,639	101,502	24,060	7,860	9,726	59,856
		True	True	TF	20	19,804	5,639	101,502	24,060	7,860	9,726	59,856
C_2H_4	JW	**False**	**False**	**-**	**28**	**60,924**	**14,383**	**402,724**	**24,636**	**24,636**	**95,420**	**258,032**
		True	False	T	28	60,924	14,378	359,450	24,046	20,992	89,060	225,352
		False	True	F	24	36,060	8,153	195,672	13,676	13,676	45,356	122,964
		True	True	TF	24	36,060	8,148	171,108	13,286	11,124	41,834	104,864
	BK	**False**	**False**	**-**	**28**	**60,924**	**14,383**	**402,724**	**45,712**	**35,240**	**43,387**	**278,385**
		True	False	T	28	60,924	14,378	359,450	36,988	30,290	57,452	234,720
		False	True	F	24	36,060	8,153	195,672	25,102	18,084	24,522	127,964
		True	True	TF	24	36,060	8,148	171,108	19,172	16,546	23,691	111,699
	P	**False**	**False**	**-**	**28**	**60,924**	**14,383**	**373,958**	**96,104**	**21,148**	**25,804**	**230,902**
		True	False	T	28	60,924	14,378	359,450	89,880	21,600	27,282	220,688
		False	True	F	24	36,060	8,153	179,366	45,768	11,508	14,280	107,810
		True	True	TF	24	36,060	8,148	171,108	42,256	11,806	15,232	101,814

Table S4. Raw circuit resource counts (continued) — circuit width, depth, total gates, and number of variational parameters for all molecules, mappers, and combinations. (-) rows (bold) serve as the baseline for reduction calculations in Table S5. Mapper abbreviations and combo codes as in Table S3.

Molecule	Mapper	Tap.	FC	Combo	W	D	G	P
H_2	JW	**False**	**False**	**-**	**4**	**60**	**85**	**3**
		True	False	T	1	1	1	1
		False	True	F	4	60	85	3
		True	True	TF	1	1	1	1
	BK	**False**	**False**	**-**	**4**	**54**	**66**	**3**
		True	False	T	1	2	2	1
		False	True	F	4	54	66	3
		True	True	TF	1	2	2	1
	P	**False**	**False**	**-**	**2**	**11**	**15**	**3**
		True	False	T	1	1	1	1
		False	True	F	2	11	15	3
		True	True	TF	1	1	1	1
LiH	JW	**False**	**False**	**-**	**12**	**7,614**	**8,808**	**92**
		True	False	T	8	1,529	1,820	34
		False	True	F	10	1,523	1,812	24
		True	True	TF	6	274	330	10
	BK	**False**	**False**	**-**	**12**	**8,231**	**9,331**	**92**
		True	False	T	8	1,801	2,113	34
		False	True	F	10	1,502	1,716	24
		True	True	TF	6	323	388	10
	P	**False**	**False**	**-**	**10**	**7,268**	**8,369**	**92**
		True	False	T	8	1,889	2,230	34
		False	True	F	8	1,332	1,597	24
		True	True	TF	6	346	435	10
HF	JW	**False**	**False**	**-**	**12**	**2,683**	**3,102**	**35**
		True	False	T	8	724	854	17
		False	True	F	10	1,499	1,774	24
		True	True	TF	6	294	358	10
	BK	**False**	**False**	**-**	**12**	**2,602**	**2,943**	**35**
		True	False	T	8	796	950	17
		False	True	F	10	1,819	2,067	24
		True	True	TF	6	369	432	10

Continued on next page

Table S4. (*continued*)

Molecule	Mapper	Tap.	FC	Combo	W	D	G	P
	P	**False**	**False**	**-**	**10**	**2,316**	**2,683**	**35**
		True	False	T	8	859	987	17
		False	True	F	8	1,254	1,487	24
		True	True	TF	6	339	400	10
BeH_2	JW	**False**	**False**	**-**	**14**	**19,821**	**22,537**	**204**
		True	False	T	9	1,962	2,263	38
		False	True	F	12	7,614	8,808	92
		True	True	TF	7	701	820	18
	BK	**False**	**False**	**-**	**14**	**18,790**	**21,434**	**204**
		True	False	T	9	2,332	2,731	38
		False	True	F	12	8,231	9,331	92
		True	True	TF	7	708	819	18
	P	**False**	**False**	**-**	**12**	**19,492**	**22,041**	**204**
		True	False	T	9	2,391	2,705	38
		False	True	F	10	7,268	8,369	92
		True	True	TF	7	819	941	18
H_2O	JW	**False**	**False**	**-**	**14**	**13,666**	**15,460**	**140**
		True	False	T	11	7,184	8,181	96
		False	True	F	12	7,738	8,893	92
		True	True	TF	9	3,472	4,026	58
	BK	**False**	**False**	**-**	**14**	**13,028**	**14,647**	**140**
		True	False	T	11	7,770	8,984	96
		False	True	F	12	8,106	9,195	92
		True	True	TF	9	3,617	4,179	58
	P	**False**	**False**	**-**	**12**	**12,842**	**14,405**	**140**
		True	False	T	11	8,306	9,393	96
		False	True	F	10	7,153	8,150	92
		True	True	TF	9	4,111	4,719	58
NH_3	JW	**False**	**False**	**-**	**16**	**34,884**	**39,069**	**315**
		True	False	T	14	31,633	35,532	315
		False	True	F	14	19,957	22,635	204
		True	True	TF	12	17,676	20,116	204
	BK	**False**	**False**	**-**	**16**	**30,485**	**34,103**	**315**

Continued on next page

Table S4. (*continued*)

Molecule	Mapper	Tap.	FC	Combo	W	D	G	P
		True	False	T	14	28,706	32,356	315
		False	True	F	14	19,855	22,423	204
		True	True	TF	12	17,414	19,836	204
	P	**False**	**False**	**-**	**14**	**34,467**	**38,300**	**315**
		True	False	T	14	35,067	38,900	315
		False	True	F	12	19,534	21,971	204
		True	True	TF	12	19,870	22,307	204
CH_4	JW	**False**	**False**	**-**	**18**	**68,742**	**76,347**	**560**
		True	False	T	16	62,938	70,088	560
		False	True	F	16	39,685	44,538	360
		True	True	TF	14	35,600	40,067	360
	BK	**False**	**False**	**-**	**18**	**62,249**	**69,812**	**560**
		True	False	T	16	57,234	64,218	560
		False	True	F	16	37,119	41,360	360
		True	True	TF	14	35,854	40,170	360
	P	**False**	**False**	**-**	**16**	**68,966**	**76,205**	**560**
		True	False	T	16	70,206	77,445	560
		False	True	F	14	39,546	44,137	360
		True	True	TF	14	40,282	44,873	360
O_2	JW	**False**	**False**	**-**	**20**	**46,926**	**51,477**	**344**
		True	False	T	15	5,109	5,705	54
		False	True	F	16	21,928	24,501	198
		True	True	TF	11	2,338	2,651	30
	BK	**False**	**False**	**-**	**20**	**43,137**	**47,465**	**344**
		True	False	T	15	5,708	6,337	54
		False	True	F	16	18,478	20,671	198
		True	True	TF	11	2,432	2,788	30
	P	**False**	**False**	**-**	**18**	**45,181**	**49,194**	**344**
		True	False	T	15	6,852	7,634	54
		False	True	F	14	20,831	23,084	198
		True	True	TF	11	2,935	3,305	30
N_2	JW	**False**	**False**	**-**	**20**	**82,633**	**90,837**	**609**
		True	False	T	16	16,487	18,481	171
		False	True	F	16	34,884	39,069	315

Continued on next page

Table S4. (*continued*)

Molecule	Mapper	Tap.	FC	Combo	W	D	G	P
		True	True	TF	12	7,980	9,091	99
	BK	**False**	**False**	**-**	**20**	**75,630**	**83,398**	**609**
		True	False	T	16	20,898	23,261	171
		False	True	F	16	30,485	34,103	315
		True	True	TF	12	9,164	10,297	99
	P	**False**	**False**	**-**	**18**	**82,381**	**89,944**	**609**
		True	False	T	16	22,682	25,047	171
		False	True	F	14	34,467	38,300	315
		True	True	TF	12	10,569	11,767	99
CO	JW	**False**	**False**	**-**	**20**	**82,633**	**90,837**	**609**
		True	False	T	17	32,017	35,659	305
		False	True	F	16	34,884	39,069	315
		True	True	TF	13	13,760	15,583	159
	BK	**False**	**False**	**-**	**20**	**75,630**	**83,398**	**609**
		True	False	T	17	33,501	37,197	305
		False	True	F	16	30,485	34,103	315
		True	True	TF	13	13,974	15,769	159
	P	**False**	**False**	**-**	**18**	**82,381**	**89,944**	**609**
		True	False	T	17	40,359	44,427	305
		False	True	F	14	34,467	38,300	315
		True	True	TF	13	17,057	19,095	159
C_2H_2	JW	**False**	**False**	**-**	**24**	**271,383**	**295,061**	**1,715**
		True	False	T	22	255,786	278,776	1,715
		False	True	F	20	117,595	129,615	875
		True	True	TF	18	108,545	119,950	875
	BK	**False**	**False**	**-**	**24**	**233,921**	**257,297**	**1,715**
		True	False	T	22	205,737	228,217	1,715
		False	True	F	20	108,495	120,770	875
		True	True	TF	18	96,460	107,864	875
	P	**False**	**False**	**-**	**22**	**275,795**	**299,114**	**1,715**
		True	False	T	22	280,317	303,636	1,715
		False	True	F	18	119,009	130,766	875
		True	True	TF	18	121,179	132,936	875

Continued on next page

Table S4. (*continued*)

Molecule	Mapper	Tap.	FC	Combo	W	D	G	P
H_2O_2	JW	**False**	**False**	**-**	**24**	**159,922**	**173,485**	**999**
		True	False	T	22	151,274	164,436	999
		False	True	F	20	82,633	90,837	609
		True	True	TF	18	76,986	84,832	609
	BK	**False**	**False**	**-**	**24**	**132,029**	**144,673**	**999**
		True	False	T	22	115,276	127,414	999
		False	True	F	20	75,630	83,398	609
		True	True	TF	18	65,888	73,176	609
	P	**False**	**False**	**-**	**22**	**160,039**	**172,588**	**999**
		True	False	T	22	162,415	174,964	999
		False	True	F	18	82,381	89,944	609
		True	True	TF	18	83,725	91,288	609
C_2H_4	JW	**False**	**False**	**-**	**28**	**586,392**	**631,404**	**3,240**
		True	False	T	25	295,668	321,618	2,002
		False	True	F	24	286,607	311,812	1,818
		True	True	TF	21	133,389	146,940	1,078
	BK	**False**	**False**	**-**	**28**	**464,839**	**511,524**	**3,240**
		True	False	T	25	271,122	298,160	2,002
		False	True	F	24	246,216	271,322	1,818
		True	True	TF	21	128,412	142,032	1,078
	P	**False**	**False**	**-**	**26**	**598,599**	**643,893**	**3,240**
		True	False	T	25	372,027	399,003	2,002
		False	True	F	22	292,163	317,389	1,818
		True	True	TF	21	172,885	187,337	1,078

Table S5. Reduction factors relative to the (-) (no tapering, no frozen core) baseline for each molecule, mapper, and combination. Values represent the ratio $v_{\text{-}}/v_{\text{combo}}$, so a value of 2.00 indicates a 2× reduction (halving of resource). Values below 1.00 (red) indicate a marginal increase relative to baseline. (-) rows are the baseline and show 1.00 by definition. Column headers: N_{so} spin orbitals, N_{sqh} Hamiltonian terms, N_{PS} Pauli strings, N_{PO} total Pauli operators, $N_X/N_Y/N_Z/N_I$ individual Pauli counts, W circuit width, D circuit depth, G total gates, P parameters. Dashes (–) indicate division by zero (e.g. $N_Y = 0$ for H_2/Parity baseline).

Molecule	Mapper	Tap.	FC	Combo	N_{so}	N_{sqh}	N_{PS}	N_{PO}	N_X	N_Y	N_Z	N_I	W	D	G	P
H_2	JW	**False**	**False**	**-**	**1.00**	**1.00**	**1.00**	**1.00**	**1.00**	**1.00**	**1.00**	**1.00**	**1.00**	**1.00**	**1.00**	**1.00**
		True	False	T	1.00	1.00	5.00	20.00	8.00	–	16.00	28.00	4.00	60.00	85.00	3.00
		False	True	F	1.00	1.00	1.00	1.00	1.00	1.00	1.00	1.00	1.00	1.00	1.00	1.00
		True	True	TF	1.00	1.00	5.00	20.00	8.00	–	16.00	28.00	4.00	60.00	85.00	3.00
	BK	**False**	**False**	**-**	**1.00**	**1.00**	**1.00**	**1.00**	**1.00**	**1.00**	**1.00**	**1.00**	**1.00**	**1.00**	**1.00**	**1.00**
		True	False	T	1.00	1.00	5.00	20.00	8.00	–	26.00	26.00	4.00	27.00	33.00	3.00
		False	True	F	1.00	1.00	1.00	1.00	1.00	–	1.00	1.00	1.00	1.00	1.00	1.00
		True	True	TF	1.00	1.00	5.00	20.00	8.00	–	26.00	26.00	4.00	27.00	33.00	3.00
	P	**False**	**False**	**-**	**1.00**	**1.00**	**1.00**	**1.00**	**1.00**	**1.00**	**1.00**	**1.00**	**1.00**	**1.00**	**1.00**	**1.00**
		True	False	T	1.00	1.00	1.67	3.33	2.00	–	4.00	4.00	2.00	11.00	15.00	3.00
		False	True	F	1.00	1.00	1.00	1.00	1.00	–	1.00	1.00	1.00	1.00	1.00	1.00
		True	True	TF	1.00	1.00	1.67	3.33	2.00	–	4.00	4.00	2.00	11.00	15.00	3.00
LiH	JW	**False**	**False**	**-**	**1.00**	**1.00**	**1.00**	**1.00**	**1.00**	**1.00**	**1.00**	**1.00**	**1.00**	**1.00**	**1.00**	**1.00**
		True	False	T	1.00	1.00	1.13	1.70	1.22	1.97	1.26	2.06	1.50	4.98	4.84	2.71
		False	True	F	1.20	2.30	2.29	2.74	2.53	2.53	2.72	2.84	1.20	5.00	4.86	3.83
		True	True	TF	1.20	2.30	2.73	5.46	3.41	6.27	3.96	7.09	2.00	27.79	26.69	9.20
	BK	**False**	**False**	**-**	**1.00**	**1.00**	**1.00**	**1.00**	**1.00**	**1.00**	**1.00**	**1.00**	**1.00**	**1.00**	**1.00**	**1.00**
		True	False	T	1.00	1.00	1.13	1.70	1.65	1.64	1.28	1.97	1.50	4.57	4.42	2.71
		False	True	F	1.20	2.30	2.29	2.74	2.81	2.43	2.54	2.90	1.20	5.48	5.44	3.83
		True	True	TF	1.20	2.30	2.73	5.46	5.10	4.52	3.39	7.81	2.00	25.48	24.05	9.20
	P	**False**	**False**	**-**	**1.00**	**1.00**	**1.00**	**1.00**	**1.00**	**1.00**	**1.00**	**1.00**	**1.00**	**1.00**	**1.00**	**1.00**
		True	False	T	1.00	1.00	1.13	1.41	1.43	1.22	1.03	1.65	1.25	3.85	3.75	2.71
		False	True	F	1.20	2.30	2.29	2.86	2.89	2.60	2.39	3.09	1.25	5.46	5.24	3.83
		True	True	TF	1.20	2.30	2.73	4.55	4.68	3.51	2.74	6.09	1.67	21.01	19.24	9.20
HF	JW	**False**	**False**	**-**	**1.00**	**1.00**	**1.00**	**1.00**	**1.00**	**1.00**	**1.00**	**1.00**	**1.00**	**1.00**	**1.00**	**1.00**
		True	False	T	1.00	1.00	1.13	1.70	1.22	1.97	1.26	2.06	1.50	3.71	3.63	2.06
		False	True	F	1.20	2.30	2.29	2.74	2.53	2.53	2.72	2.84	1.20	1.79	1.75	1.46
		True	True	TF	1.20	2.30	2.73	5.46	3.41	6.27	3.96	7.09	2.00	9.13	8.66	3.50
	BK	**False**	**False**	**-**	**1.00**	**1.00**	**1.00**	**1.00**	**1.00**	**1.00**	**1.00**	**1.00**	**1.00**	**1.00**	**1.00**	**1.00**
		True	False	T	1.00	1.00	1.13	1.70	1.65	1.64	1.28	1.97	1.50	3.27	3.10	2.06
		False	True	F	1.20	2.30	2.29	2.74	2.81	2.43	2.54	2.90	1.20	1.43	1.42	1.46

Continued on next page

Table S5. (*continued*)

Molecule	Mapper	Tap.	FC	Combo	N_{so}	N_{sqh}	N_{PS}	N_{PO}	N_X	N_Y	N_Z	N_I	W	D	G	P
		True	True	TF	1.20	2.30	2.73	5.46	5.10	4.52	3.39	7.81	2.00	7.05	6.81	3.50
	P	**False**	**False**	**-**	**1.00**	**1.00**	**1.00**	**1.00**	**1.00**	**1.00**	**1.00**	**1.00**	**1.00**	**1.00**	**1.00**	**1.00**
		True	False	T	1.00	1.00	1.13	1.41	1.43	1.22	1.03	1.65	1.25	2.70	2.72	2.06
		False	True	F	1.20	2.30	2.29	2.86	2.89	2.60	2.39	3.09	1.25	1.85	1.80	1.46
		True	True	TF	1.20	2.30	2.73	4.55	4.68	3.51	2.74	6.09	1.67	6.83	6.71	3.50
BeH_2	JW	**False**	**False**	**-**	**1.00**	**1.00**	**1.00**	**1.00**	**1.00**	**1.00**	**1.00**	**1.00**	**1.00**	**1.00**	**1.00**	**1.00**
		True	False	T	1.00	1.00	1.12	1.74	1.33	1.89	1.20	2.19	1.56	10.10	9.96	5.37
		False	True	F	1.17	1.99	2.04	2.38	2.24	2.24	2.40	2.42	1.17	2.60	2.56	2.22
		True	True	TF	1.17	1.99	2.49	4.97	3.40	5.07	3.25	6.84	2.00	28.28	27.48	11.33
	BK	**False**	**False**	**-**	**1.00**	**1.00**	**1.00**	**1.00**	**1.00**	**1.00**	**1.00**	**1.00**	**1.00**	**1.00**	**1.00**	**1.00**
		True	False	T	1.00	1.00	1.12	1.74	1.61	1.62	0.95	2.35	1.56	8.06	7.85	5.37
		False	True	F	1.17	1.99	2.04	2.38	2.22	2.46	1.89	2.58	1.17	2.28	2.30	2.22
		True	True	TF	1.17	1.99	2.49	4.97	4.51	4.89	2.84	6.46	2.00	26.54	26.17	11.33
	P	**False**	**False**	**-**	**1.00**	**1.00**	**1.00**	**1.00**	**1.00**	**1.00**	**1.00**	**1.00**	**1.00**	**1.00**	**1.00**	**1.00**
		True	False	T	1.00	1.00	1.12	1.49	1.72	1.09	0.92	1.79	1.33	8.15	8.15	5.37
		False	True	F	1.17	1.99	2.04	2.44	2.54	2.21	2.10	2.56	1.20	2.68	2.63	2.22
		True	True	TF	1.17	1.99	2.49	4.26	4.92	2.66	2.37	5.71	1.71	23.80	23.42	11.33
H_2O	JW	**False**	**False**	**-**	**1.00**	**1.00**	**1.00**	**1.00**	**1.00**	**1.00**	**1.00**	**1.00**	**1.00**	**1.00**	**1.00**	**1.00**
		True	False	T	1.00	1.00	1.04	1.32	1.07	1.53	1.06	1.48	1.27	1.90	1.89	1.46
		False	True	F	1.17	1.97	1.97	2.30	2.08	2.08	2.35	2.37	1.17	1.77	1.74	1.52
		True	True	TF	1.17	1.97	2.08	3.23	2.25	3.49	2.60	3.80	1.56	3.94	3.84	2.41
	BK	**False**	**False**	**-**	**1.00**	**1.00**	**1.00**	**1.00**	**1.00**	**1.00**	**1.00**	**1.00**	**1.00**	**1.00**	**1.00**	**1.00**
		True	False	T	1.00	1.00	1.04	1.32	1.20	1.30	1.06	1.47	1.27	1.68	1.63	1.46
		False	True	F	1.17	1.97	1.97	2.30	1.94	2.06	2.01	2.60	1.17	1.61	1.59	1.52
		True	True	TF	1.17	1.97	2.08	3.23	2.82	3.07	2.31	3.83	1.56	3.60	3.50	2.41
	P	**False**	**False**	**-**	**1.00**	**1.00**	**1.00**	**1.00**	**1.00**	**1.00**	**1.00**	**1.00**	**1.00**	**1.00**	**1.00**	**1.00**
		True	False	T	1.00	1.00	1.04	1.13	1.18	1.03	0.97	1.19	1.09	1.55	1.53	1.46
		False	True	F	1.17	1.97	1.97	2.37	2.38	2.17	2.06	2.49	1.20	1.80	1.77	1.52
		True	True	TF	1.17	1.97	2.08	2.77	2.95	2.24	2.05	3.10	1.33	3.12	3.05	2.41
NH_3	JW	**False**	**False**	**-**	**1.00**	**1.00**	**1.00**	**1.00**	**1.00**	**1.00**	**1.00**	**1.00**	**1.00**	**1.00**	**1.00**	**1.00**
		True	False	T	1.00	1.00	1.00	1.14	1.01	1.26	0.98	1.22	1.14	1.10	1.10	1.00
		False	True	F	1.14	1.54	1.55	1.77	1.58	1.58	1.81	1.84	1.14	1.75	1.73	1.54
		True	True	TF	1.14	1.54	1.55	2.07	1.59	2.07	1.75	2.35	1.33	1.97	1.94	1.54

Continued on next page

Table S5. (*continued*)

Molecule	Mapper	Tap.	FC	Combo	N_{so}	N_{sqh}	N_{PS}	N_{PO}	N_X	N_Y	N_Z	N_I	W	D	G	P
	BK	**False**	**False**	**-**	**1.00**	**1.00**	**1.00**	**1.00**	**1.00**	**1.00**	**1.00**	**1.00**	**1.00**	**1.00**	**1.00**	**1.00**
		True	False	T	1.00	1.00	1.00	1.14	1.00	1.00	1.18	1.20	1.14	1.06	1.05	1.00
		False	True	F	1.14	1.54	1.55	1.77	1.36	1.36	2.09	1.92	1.14	1.54	1.52	1.54
		True	True	TF	1.14	1.54	1.55	2.07	1.55	1.67	2.12	2.31	1.33	1.75	1.72	1.54
	P	**False**	**False**	**-**	**1.00**	**1.00**	**1.00**	**1.00**	**1.00**	**1.00**	**1.00**	**1.00**	**1.00**	**1.00**	**1.00**	**1.00**
		True	False	T	1.00	1.00	1.00	1.00	1.00	1.00	1.00	1.00	1.00	0.98	0.98	1.00
		False	True	F	1.14	1.54	1.55	1.81	1.78	1.66	1.59	1.91	1.17	1.76	1.74	1.54
		True	True	TF	1.14	1.54	1.55	1.81	1.78	1.66	1.59	1.91	1.17	1.73	1.72	1.54
CH_4	JW	**False**	**False**	**-**	**1.00**	**1.00**	**1.00**	**1.00**	**1.00**	**1.00**	**1.00**	**1.00**	**1.00**	**1.00**	**1.00**	**1.00**
		True	False	T	1.00	1.00	1.00	1.12	1.01	1.22	0.98	1.19	1.12	1.09	1.09	1.00
		False	True	F	1.12	1.46	1.47	1.65	1.50	1.50	1.68	1.70	1.12	1.73	1.71	1.56
		True	True	TF	1.12	1.46	1.47	1.89	1.50	1.90	1.60	2.09	1.29	1.93	1.91	1.56
	BK	**False**	**False**	**-**	**1.00**	**1.00**	**1.00**	**1.00**	**1.00**	**1.00**	**1.00**	**1.00**	**1.00**	**1.00**	**1.00**	**1.00**
		True	False	T	1.00	1.00	1.00	1.12	1.10	1.12	1.03	1.16	1.12	1.09	1.09	1.00
		False	True	F	1.12	1.46	1.47	1.65	1.77	1.66	1.67	1.62	1.12	1.68	1.69	1.56
		True	True	TF	1.12	1.46	1.47	1.89	1.77	1.66	1.90	1.97	1.29	1.74	1.74	1.56
	P	**False**	**False**	**-**	**1.00**	**1.00**	**1.00**	**1.00**	**1.00**	**1.00**	**1.00**	**1.00**	**1.00**	**1.00**	**1.00**	**1.00**
		True	False	T	1.00	1.00	1.00	1.00	1.00	1.00	1.00	1.00	1.00	0.98	0.98	1.00
		False	True	F	1.12	1.46	1.47	1.68	1.66	1.56	1.50	1.75	1.14	1.74	1.73	1.56
		True	True	TF	1.12	1.46	1.47	1.68	1.66	1.56	1.50	1.75	1.14	1.71	1.70	1.56
O_2	JW	**False**	**False**	**-**	**1.00**	**1.00**	**1.00**	**1.00**	**1.00**	**1.00**	**1.00**	**1.00**	**1.00**	**1.00**	**1.00**	**1.00**
		True	False	T	1.00	1.00	1.00	1.34	1.20	1.50	0.97	1.55	1.33	9.18	9.02	6.37
		False	True	F	1.25	2.73	2.71	3.39	2.87	2.87	3.53	3.51	1.25	2.14	2.10	1.74
		True	True	TF	1.25	2.73	2.75	4.99	3.75	4.92	3.23	6.53	1.82	20.07	19.42	11.47
	BK	**False**	**False**	**-**	**1.00**	**1.00**	**1.00**	**1.00**	**1.00**	**1.00**	**1.00**	**1.00**	**1.00**	**1.00**	**1.00**	**1.00**
		True	False	T	1.00	1.00	1.00	1.34	1.51	1.29	0.68	1.68	1.33	7.56	7.49	6.37
		False	True	F	1.25	2.73	2.71	3.39	3.81	3.51	3.05	3.39	1.25	2.33	2.30	1.74
		True	True	TF	1.25	2.73	2.75	4.99	4.72	4.04	2.57	6.83	1.82	17.74	17.02	11.47
	P	**False**	**False**	**-**	**1.00**	**1.00**	**1.00**	**1.00**	**1.00**	**1.00**	**1.00**	**1.00**	**1.00**	**1.00**	**1.00**	**1.00**
		True	False	T	1.00	1.00	1.00	1.21	1.45	0.78	0.57	1.49	1.20	6.59	6.44	6.37
		False	True	F	1.25	2.73	2.71	3.49	3.58	3.00	2.77	3.69	1.29	2.17	2.13	1.74
		True	True	TF	1.25	2.73	2.75	4.50	6.03	2.34	1.77	6.17	1.64	15.39	14.88	11.47
N_2	JW	**False**	**False**	**-**	**1.00**	**1.00**	**1.00**	**1.00**	**1.00**	**1.00**	**1.00**	**1.00**	**1.00**	**1.00**	**1.00**	**1.00**

Continued on next page

Table S5. (*continued*)

Molecule	Mapper	Tap.	FC	Combo	N_{so}	N_{sqh}	N_{PS}	N_{PO}	N_X	N_Y	N_Z	N_I	W	D	G	P
		True	False	T	1.00	1.00	1.00	1.25	1.16	1.37	0.92	1.42	1.25	5.01	4.92	3.56
		False	True	F	1.25	2.51	2.51	3.13	2.59	2.59	3.29	3.27	1.25	2.37	2.33	1.93
		True	True	TF	1.25	2.51	2.51	4.18	3.16	3.87	3.01	5.13	1.67	10.36	9.99	6.15
	BK	**False**	**False**	**-**	**1.00**	**1.00**	**1.00**	**1.00**	**1.00**	**1.00**	**1.00**	**1.00**	**1.00**	**1.00**	**1.00**	**1.00**
		True	False	T	1.00	1.00	1.00	1.25	1.38	1.28	0.60	1.59	1.25	3.62	3.59	3.56
		False	True	F	1.25	2.51	2.51	3.13	3.55	3.18	2.84	3.12	1.25	2.48	2.45	1.93
		True	True	TF	1.25	2.51	2.51	4.18	4.15	3.74	2.05	5.61	1.67	8.25	8.10	6.15
	P	**False**	**False**	**-**	**1.00**	**1.00**	**1.00**	**1.00**	**1.00**	**1.00**	**1.00**	**1.00**	**1.00**	**1.00**	**1.00**	**1.00**
		True	False	T	1.00	1.00	1.00	1.12	1.26	0.80	0.69	1.27	1.12	3.63	3.59	3.56
		False	True	F	1.25	2.51	2.51	3.22	3.25	2.76	2.59	3.42	1.29	2.39	2.35	1.93
		True	True	TF	1.25	2.51	2.51	3.76	4.12	2.55	1.99	4.55	1.50	7.79	7.64	6.15
CO	JW	**False**	**False**	**-**	**1.00**	**1.00**	**1.00**	**1.00**	**1.00**	**1.00**	**1.00**	**1.00**	**1.00**	**1.00**	**1.00**	**1.00**
		True	False	T	1.00	1.00	1.00	1.18	1.08	1.29	0.98	1.27	1.18	2.58	2.55	2.00
		False	True	F	1.25	2.49	2.50	3.13	2.60	2.60	3.30	3.25	1.25	2.37	2.33	1.93
		True	True	TF	1.25	2.49	2.50	3.85	2.88	3.62	3.12	4.47	1.54	6.01	5.83	3.83
	BK	**False**	**False**	**-**	**1.00**	**1.00**	**1.00**	**1.00**	**1.00**	**1.00**	**1.00**	**1.00**	**1.00**	**1.00**	**1.00**	**1.00**
		True	False	T	1.00	1.00	1.00	1.18	1.33	1.21	0.71	1.34	1.18	2.26	2.24	2.00
		False	True	F	1.25	2.49	2.50	3.13	3.60	3.08	2.88	3.10	1.25	2.48	2.45	1.93
		True	True	TF	1.25	2.49	2.50	3.85	3.76	3.55	2.27	4.74	1.54	5.41	5.29	3.83
	P	**False**	**False**	**-**	**1.00**	**1.00**	**1.00**	**1.00**	**1.00**	**1.00**	**1.00**	**1.00**	**1.00**	**1.00**	**1.00**	**1.00**
		True	False	T	1.00	1.00	1.00	1.06	1.14	0.91	0.76	1.13	1.06	2.04	2.02	2.00
		False	True	F	1.25	2.49	2.50	3.22	3.28	2.72	2.59	3.41	1.29	2.39	2.35	1.93
		True	True	TF	1.25	2.49	2.50	3.46	3.86	2.41	1.94	4.07	1.38	4.83	4.71	3.83
C_2H_2	JW	**False**	**False**	**-**	**1.00**	**1.00**	**1.00**	**1.00**	**1.00**	**1.00**	**1.00**	**1.00**	**1.00**	**1.00**	**1.00**	**1.00**
		True	False	T	1.00	1.00	1.00	1.09	1.01	1.20	0.95	1.15	1.09	1.06	1.06	1.00
		False	True	F	1.20	1.96	2.02	2.42	2.05	2.05	2.51	2.49	1.20	2.31	2.28	1.96
		True	True	TF	1.20	1.96	2.02	2.69	2.08	2.55	2.39	2.93	1.33	2.50	2.46	1.96
	BK	**False**	**False**	**-**	**1.00**	**1.00**	**1.00**	**1.00**	**1.00**	**1.00**	**1.00**	**1.00**	**1.00**	**1.00**	**1.00**	**1.00**
		True	False	T	1.00	1.00	1.00	1.09	1.24	1.08	1.16	1.06	1.09	1.14	1.13	1.00
		False	True	F	1.20	1.96	2.02	2.42	2.19	2.09	2.23	2.58	1.20	2.16	2.13	1.96
		True	True	TF	1.20	1.96	2.02	2.69	2.63	2.33	2.40	2.84	1.33	2.43	2.39	1.96
	P	**False**	**False**	**-**	**1.00**	**1.00**	**1.00**	**1.00**	**1.00**	**1.00**	**1.00**	**1.00**	**1.00**	**1.00**	**1.00**	**1.00**
		True	False	T	1.00	1.00	1.00	1.00	1.00	1.00	1.00	1.00	1.00	0.98	0.99	1.00
		False	True	F	1.20	1.96	2.02	2.47	2.50	2.09	2.08	2.57	1.22	2.32	2.29	1.96

Continued on next page

Table S5. (*continued*)

Molecule	Mapper	Tap.	FC	Combo	N_{so}	N_{sqh}	N_{PS}	N_{PO}	N_X	N_Y	N_Z	N_I	W	D	G	P
		True	True	TF	1.20	1.96	2.02	2.47	2.50	2.09	2.08	2.57	1.22	2.28	2.25	1.96
H_2O_2	JW	**False**	**False**	**-**	**1.00**	**1.00**	**1.00**	**1.00**	**1.00**	**1.00**	**1.00**	**1.00**	**1.00**	**1.00**	**1.00**	**1.00**
		True	False	T	1.00	1.00	1.00	1.09	1.01	1.17	0.95	1.15	1.09	1.06	1.06	1.00
		False	True	F	1.20	1.99	1.93	2.32	1.96	1.96	2.37	2.39	1.20	1.94	1.91	1.64
		True	True	TF	1.20	1.99	1.93	2.57	1.98	2.41	2.26	2.82	1.33	2.08	2.05	1.64
	BK	**False**	**False**	**-**	**1.00**	**1.00**	**1.00**	**1.00**	**1.00**	**1.00**	**1.00**	**1.00**	**1.00**	**1.00**	**1.00**	**1.00**
		True	False	T	1.00	1.00	1.00	1.09	1.24	1.07	1.15	1.06	1.09	1.15	1.14	1.00
		False	True	F	1.20	1.99	1.93	2.32	2.08	1.99	2.12	2.47	1.20	1.75	1.73	1.64
		True	True	TF	1.20	1.99	1.93	2.57	2.49	2.22	2.27	2.72	1.33	2.00	1.98	1.64
	P	**False**	**False**	**-**	**1.00**	**1.00**	**1.00**	**1.00**	**1.00**	**1.00**	**1.00**	**1.00**	**1.00**	**1.00**	**1.00**	**1.00**
		True	False	T	1.00	1.00	1.00	1.00	1.00	1.00	1.00	1.00	1.00	0.99	0.99	1.00
		False	True	F	1.20	1.99	1.93	2.36	2.36	2.00	2.00	2.46	1.22	1.94	1.92	1.64
		True	True	TF	1.20	1.99	1.93	2.36	2.36	2.00	2.00	2.46	1.22	1.91	1.89	1.64
C_2H_4	JW	**False**	**False**	**-**	**1.00**	**1.00**	**1.00**	**1.00**	**1.00**	**1.00**	**1.00**	**1.00**	**1.00**	**1.00**	**1.00**	**1.00**
		True	False	T	1.00	1.00	1.00	1.12	1.02	1.17	1.07	1.15	1.12	1.98	1.96	1.62
		False	True	F	1.17	1.69	1.76	2.06	1.80	1.80	2.10	2.10	1.17	2.05	2.02	1.78
		True	True	TF	1.17	1.69	1.77	2.35	1.85	2.21	2.28	2.46	1.33	4.40	4.30	3.01
	BK	**False**	**False**	**-**	**1.00**	**1.00**	**1.00**	**1.00**	**1.00**	**1.00**	**1.00**	**1.00**	**1.00**	**1.00**	**1.00**	**1.00**
		True	False	T	1.00	1.00	1.00	1.12	1.24	1.16	0.76	1.19	1.12	1.71	1.72	1.62
		False	True	F	1.17	1.69	1.76	2.06	1.82	1.95	1.77	2.18	1.17	1.89	1.89	1.78
		True	True	TF	1.17	1.69	1.77	2.35	2.38	2.13	1.83	2.49	1.33	3.62	3.60	3.01
	P	**False**	**False**	**-**	**1.00**	**1.00**	**1.00**	**1.00**	**1.00**	**1.00**	**1.00**	**1.00**	**1.00**	**1.00**	**1.00**	**1.00**
		True	False	T	1.00	1.00	1.00	1.04	1.07	0.98	0.95	1.05	1.04	1.61	1.61	1.62
		False	True	F	1.17	1.69	1.76	2.08	2.10	1.84	1.81	2.14	1.18	2.05	2.03	1.78
		True	True	TF	1.17	1.69	1.77	2.19	2.27	1.79	1.69	2.27	1.24	3.46	3.44	3.01